Science Advances
AAAS

Supplementary Materials for

Perovskite retinomorphic image sensor for embodied intelligent vision

Zhilong He *et al.*

Corresponding author: Wu Bin Ying, yingwubin@kaist.ac.kr; Zhibin Yang, zhibinyang@sjtu.edu.cn; Zhang Zhang, zhangzhang@hfut.edu.cn; Gang Liu, gang.liu@sjtu.edu.cn

Sci. Adv. **11**, eads2834 (2025)
DOI: 10.1126/sciadv.ads2834

The PDF file includes:

Other Supplementary Material for this manuscript includes the following:

Supplementary Text

1. Material characterization of NBG perovskite

As shown in Fig. S1a, the thicknesses of the $FA_{0.8}Cs_{0.2}Pb_{0.5}Sn_{0.5}I_3$ thin films spin-coated from the perovskite precursor solutions onto ITO substrates were measured by a step profiler. Before measurements, the perovskite thin films were scratched by a metal blade completely to uncover the substrates. As reflected by the heights of the scratched slits, the thicknesses of the perovskite thin films are around 600 nm, 800 nm and 1000 nm for samples prepared from precursor solutions with the concentrations of 1.4 M, 1.6 M and 1.8 M, respectively.

The XRD patterns of these perovskite films were monitored to elucidate the crystallinity of the perovskite. It is apparent that all perovskite films display similar crystallographic orientation

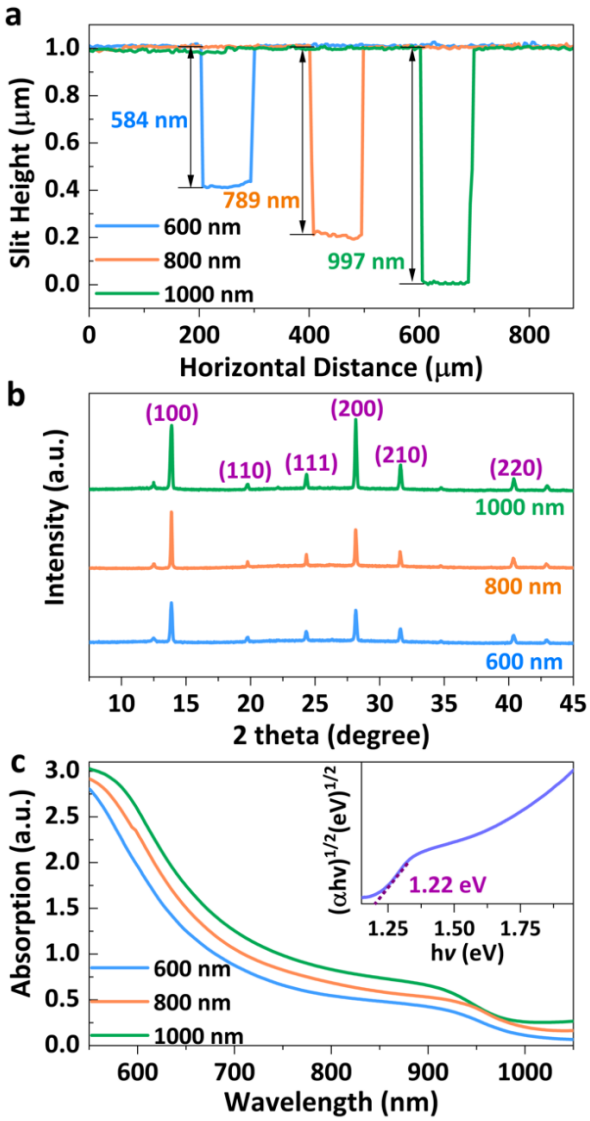

Fig. S1. Thicknesses, crystallinity and spectral absorption measurements. (a) Thicknesses, (b) XRD patterns and (c) absorption spectra of $FA_{0.8}Cs_{0.2}Pb_{0.5}Sn_{0.5}I_3$ films prepared from perovskite precursor solutions of different concentrations.

and high crystallinity (Fig. S1b), confirming the conversion of the precursor to desired perovskite phase (*46*). Manifestly, the strong peaks at 14.3° and 28.5° suggests preferred crystal growth and orientation along the (h00) crystallographic planes. It benefits the transport of charge carriers and inhibition of carrier recombination that are favorable for high performance photodetectors.

On the other hand, the absorption spectra of these perovskite thin films show strong absorbance and thickness-dependence in the broad VIS-NIR spectrum of 550 nm to 1050 nm (Fig. S1c). Strong absorption is a prerequisite for achieving high-efficiency photodetectors, while the enhancement in the absorbance with the increment of perovskite film thickness indicates a better photon harvesting ability of thicker perovskite films in long wavelength range. According to the following equation

$$\alpha(hc/\lambda) = A(hc/\lambda - E_g)^{n/2} \quad (1)$$

where α and A represent the absorption coefficient and material characteristic constant, h is the Planck constant (6.63×10^{-34} J·s), λ is the absorption edge of the perovskite film (1020 nm), and n is 1 for direction transition in perovskite, the optical bandgap (E_g) of $FA_{0.8}Cs_{0.2}Pb_{0.5}Sn_{0.5}I_3$ is derived as 1.22 eV (inset of Fig. S1c). It is in good accordance with our design of narrow bandgap perovskite by the inclusion of Sn components in the composition.

XPS analysis was conducted to verify the chemical composition of the perovskite sample. As depicted in Fig. S2a, the wide-scan XPS spectrum confirms the existence of all C, N, Cs, Pb, Sn, and I elements in the as-prepared $FA_{0.8}Cs_{0.2}Pb_{0.5}Sn_{0.5}I_3$ thin film. The energy band diagram is also determined by UPS measurements. As shown, the secondary electron cut-off edge ($E_{cut\text{-}off}$) and Fermi edge (E_{Fermi}) energies are 16.78 eV and 0.92 eV, respectively (Fig. S2b). Thus, the valance band (E_{VB}) and conduction band (E_{CB}) energy levels of $FA_{0.8}Cs_{0.2}Pb_{0.5}Sn_{0.5}I_3$ are derived as -5.34 eV and -4.12 eV, respectively, according to the following equations

$$E_{VB} = 21.2 - \left(E_{cut-off} - E_{Fermi}\right) \quad (2)$$

$$E_{CB} = E_{VB} + E_g \quad (3)$$

Note that the XPS and UPS spectra for $FA_{0.8}Cs_{0.2}Pb_{0.5}Sn_{0.5}I_3$ films of different thicknesses exhibit similar lineshapes.

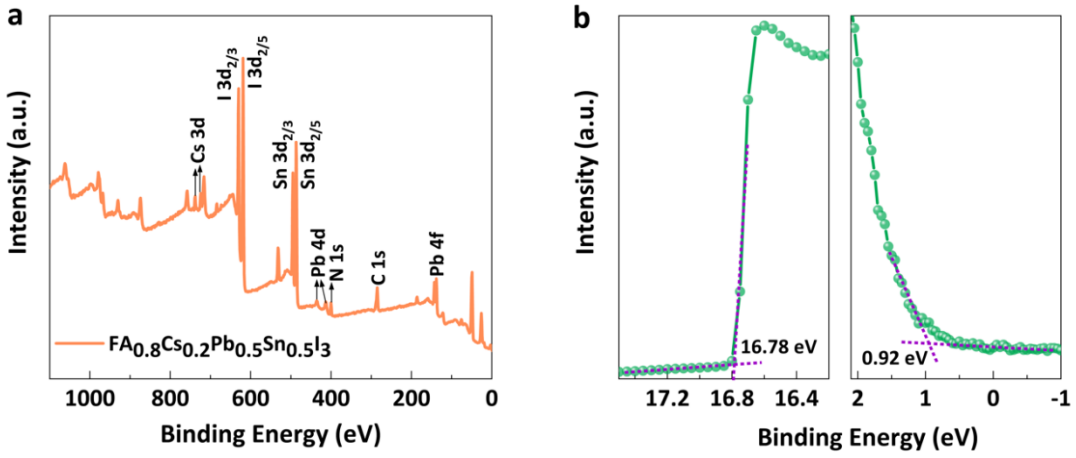

Fig. S2. Chemical composition and energy band measurements. (a) XPS and (b) UPS spectra of the as-prepared 800 nm thick $FA_{0.8}Cs_{0.2}Pb_{0.5}Sn_{0.5}I_3$ film.

Top-view SEM images of the NBG perovskite films with different thicknesses were recorded in Fig. S3a-c. Apparently, the average grain size of the perovskite increases with the increment of perovskite film thickness. Larger perovskite crystallite size with low-density grain boundaries can facilitate the suppression of hole-electron pair recombination. Note that pinholes can be observed in the 600 nm thick sample around the grain boundaries, which may be attributed to the evaporation of excess solvents from the precursor film during annealing. As for the 1000 nm thick sample, grains with inhomogeneous sizes and incompletely formed grains can be found. Such less uniform surface morphology of the perovskite thin film plays an adverse effect on carrier transport and thus device performance. Comparatively, compact morphology without obvious defects is exhibited in 800 nm thick high-quality perovskite film. Fig. S3d-f show the cross-sectional images of perovskite films with various thicknesses. In good agreement with their corresponding top-view SEM images, perovskite film with the thickness of 800 nm shows pinhole-free compact structure that is favorable for decreasing leaking dark current and improving photodetecting capability of perovskite-based devices.

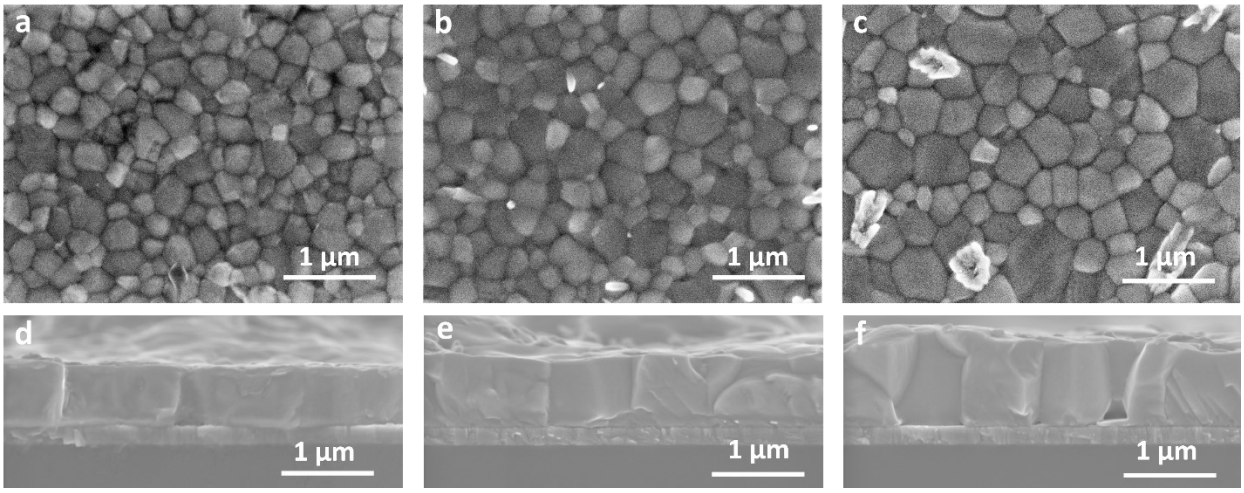

Fig. S3. Morphology characterization. (a-c) Top-view and (d-f) cross-sectional SEM photographs of $FA_{0.8}Cs_{0.2}Pb_{0.5}Sn_{0.5}I_3$ films with thicknesses of 600 nm, 800 nm and 1000 nm, respectively.

2. Design and characterization of 4096-pixel amorphous silicon thin film transistor panel

The dark and photo currents of most state-of-the-art NBG perovskite photodetectors are in the range of 10^{-9} mA/cm^2 to 10^{-2} mA/cm^2, when being scanned in dc sweeps between ±1 V under AM 1.5G illumination. In order to drive the perovskite devices to work properly, as well as perform functions of selecting, photoresponse modulating and amplifying, transistors with leakage current less than 1 nA, threshold voltage below 10 V and ON/OFF ratio over 10^4 should be included to construct high performance retinomorphic image sensor array with a one transistor-one photodetector (1T-1PD) geometry. The large photodetecting area, commendable fill factor and superior integrating capability of 1T-1PD cell, in the meanwhile, benefit the enhancement of areal efficiency of the photoconversion process. Considering the outstanding technical maturity and accessibility, in this work we utilize the amorphous silicon thin film transistor (α-Si TFT) technology to design and implement 4096-pixel transistor array panel in Tianma standard G4.5 6-mask fab process.

As shown in Fig. 2a, the α-Si TFT panel consists of a central 4096-pixel array region with gate electrode (select) lines and source electrode (operate) lines connected to the bonding area for the external flexible printed cable (FPC) connections, a common electrode area reserved for the universal cathode of superimposed photodetectors, and test groups (TEGs) for TFT characterization. The overall size of each pixel is 2.5×10^{-3} cm^2 (500 μm × 500 μm). The active area of the perovskite devices, which is defined by the bottom ITO electrode, is 9×10^{-4} cm^2 (300 μm × 300 μm). As such, the fill factor and integration density of the 1T-1PD pixel are calculated as 9×10^{-4} cm^2/2.5×10^{-3} cm^2=0.36 and 1 pixel/500 μm= 2 pixel/mm, respectively. The TFT device is located at the lower left corner of each pixel. The source electrode has a concave shape and serves as data terminal to read the current response of the photodetector device. The drain electrode interdigitates with the source electrode, defining a 100 μm width and a 10 μm length of the TFT channel.

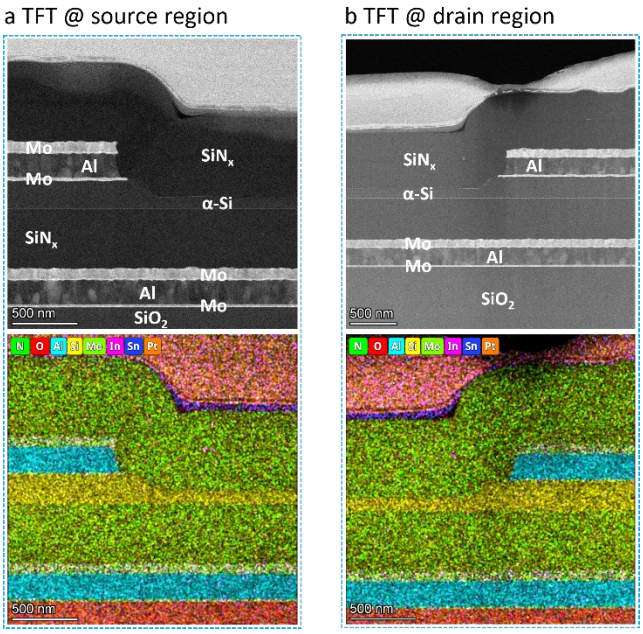

Fig. S4. Cross-sectional STEM images of the α-Si TFT. (a) source and (b) drain regions, wherein the amorphous silicon semiconductor layers are differentiated by grey dash lines.

Cross-sectional view of the 1T-1PD cell reveal that TFT devices are fabricated on glass substrate (Fig. S4a and S4b). The gate electrode is composed of trilayer metals of Mo, Al and Mo with thicknesses of 20 nm, 180 nm and 80 nm, wherein Mo serves as protective layer to avoid Al conducting layer from oxidation. Insulating silicon nitride SiN_x with the thickness of 430 nm is used as dielectric. The 100 nm thick α-Si layer is deposited on SiN_x as semiconductor channel, while islands of heavily doped n^+ Si are included to improve the metal/ semiconductor contact quality, respectively. Both source and drain electrodes are made of trilayer metals of Mo/Al/Mo with the thicknesses of 20 nm, 180 nm and 80 nm. Another SiN_x layer with the thickness of 430 nm is deposited on top of the source, drain and semiconductor channel for passivation. The ITO electrode for photodetector device is 75 nm thick and connected to the TFT drain through SiN_x vias. Finally, another 430 nm thick SiN_x passivation layer is deposited on top of the entire sample, with opening windows of 300 μm×300 μm over the ITO electrodes for the construction of perovskite-based photodetector devices. As described in the device fabrication section, the PEDOT:PSS hole transporting layer was patterned through standard photolithography and aqueous etching processes into isolated islands with pad size and pitch of 350 μm and 150 μm respectively to avoid potential voltage stimulus cross-talk and mis-operation by the neighbor TFT devices.

The electrical characteristics of the α-Si TFT devices are displayed in Fig. S5. The transfer curves of Fig. S5a reveal that the leakage current, threshold voltage (V_{TH}) and subthreshold swing (SS) are as low as ~ 10 pA, 3.4 V (read at V_{DS}=1 V and I=W/L×1 nA=10 nA) and 2.5 V/dec (V_{DS}=10 V), respectively, which promise fast, low-power and low-noise operations of the TFT devices. When a driving voltage (V_G) of 10 V is employed, the transistor can be effectively switched on, with ON/OFF ratio reaching at 2.93×10^3 at V_{DS}=0.1 V, 2.79×10^4 at V_{DS}=1 V and 1.26×10^5 at V_{DS}=10 V for proper selection and photoresponse amplification of the photodetector. When the driving voltage is 20 V, the ON/OFF ratio increases to 6.67×10^3 at V_{DS}=0.1 V, 7.89×10^4 at V_{DS}=1 V and 7.88×10^5 at V_{DS}=10 V. On the other hand, the output characteristics of the α-Si TFT device in Fig. S5b present obvious pinch-off and current saturation. The steep slopes of the linear region indicate that the photocurrent (thus photoresponsivity) of the 1T-1PD cell can be effective modulated for adaptive image sensing in dim light environment, as well as for synaptic weight updating according to the pretrained neural network algorithm.

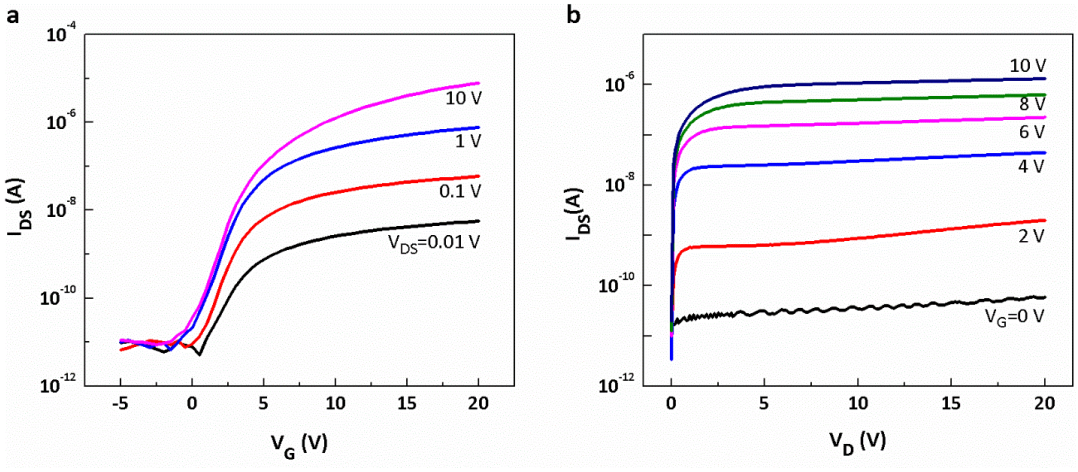

Fig. S5. Electrical characteristics of the α-Si thin film transistor. (a) Transfer and (b) output curves.

3. Fundamental photodetecting performance of perovskite device

As discussed in the material characterization section, $FA_{0.8}Cs_{0.2}Pb_{0.5}Sn_{0.5}I_3$ exhibits strong film thickness dependence of the optical absorption, crystallinity and morphology, which may in turn significantly influence its photodetecting performance. In this work, inverted photodetectors with device configuration of ITO/PEDOT:PSS/perovskite/C_{60}/BCP/Au were fabricated. Fig. S6 plots schematic energy band diagram of the device. The appropriate energy level alignment of the NBG perovskite, HTL and ETL could efficaciously facilitate separation and transfer of the photo-generated charge carriers, while suppress their recombination in the meanwhile. In good accordance with the enhanced absorption in the NIR region, higher photocurrent density and short-circuit currents are also recorded in devices constructed from thicker perovskite films. As depicted in the current density-voltage (J-V) characteristics of Fig. S7a, the short-circuit current densities (J_{sc}) are 27.98 mA/cm^2, 29.76 mA/cm^2 and 30.37 mA/cm^2 for devices with 0.08 cm^2 active area and 600 nm, 800 nm, and 1000 nm thick perovskite layers, respectively, under AM 1.5G (100 mW/cm^2) illumination. The open-circuit voltages (V_{oc}) of these devices are 0.77 V, 0.76 V and 0.66 V. The dark current, which determines the detectivity of the photodetectors, also decreases with increase in the perovskite layer thickness, especially under negative biases (Fig. S7b). It can be understood in terms of larger perovskite grain size and less amount of grain boundaries that reduce the occurrence of current leaking at structural and compositional defects.

Considering the overall performance of perovskite-based photodetectors, the optimal thickness of perovskite layer is fixed as 800 nm for the following studies. Fig. S8a displays the J-V curve of the 800 nm thick perovskite device recorded in dark environment and under AM 1.5 G illumination, with the respective current densities of 1.73×10^{-6} mA/cm^2 and 29.89 mA/cm^2 when read at 0 V. The light/dark current ratio of the $FA_{0.8}Cs_{0.2}Pb_{0.5}Sn_{0.5}I_3$ photodetector is derived as 1.72×10^7.

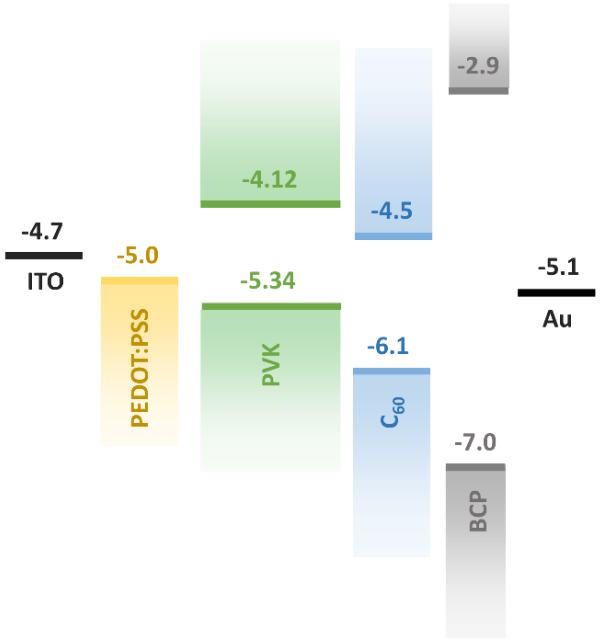

Fig. S6. Energy band diagrams. The inverted $FA_{0.8}Cs_{0.2}Pb_{0.5}Sn_{0.5}I_3$ based photodetectors with the configuration of ITO/PEDOT:PSS/perovskite/C_{60}/BCP/Au.

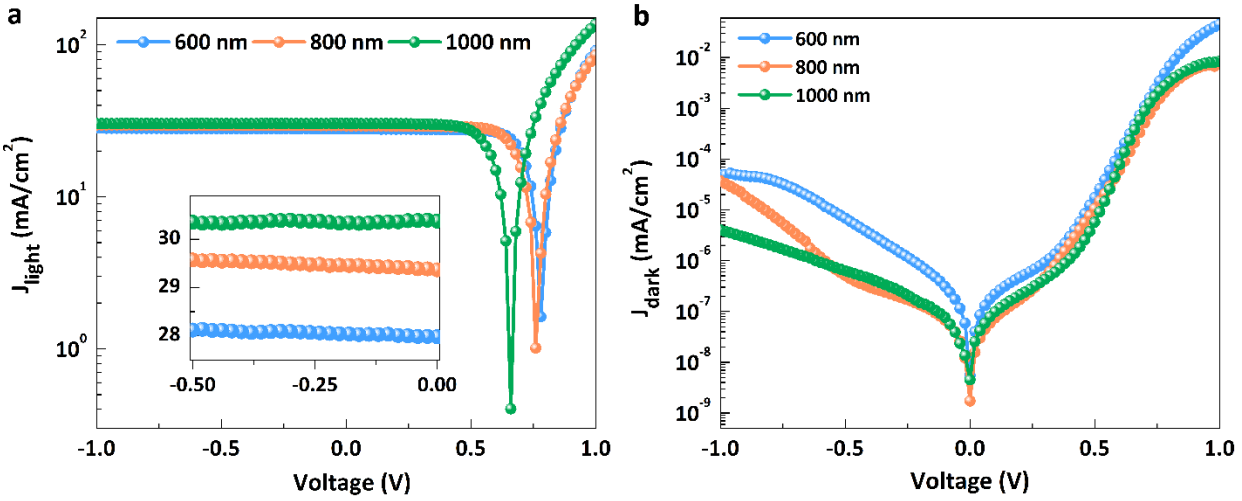

Fig. S7. J-V characteristics of the perovskite photodetectors. The $FA_{0.8}Cs_{0.2}Pb_{0.5}Sn_{0.5}I_3$ photodetectors having different perovskite layer thicknesses of 600, 800 and 100 nm, recorded (a) under AM 1.5G illumination (100 mW/cm^2) and (b) in dark condition, respectively.

External quantum efficiency (*EQE*), photoresponsivity (*R*) and specific detectivity (D^*) are employed to further evaluate the photoelectric conversion ability of the present $FA_{0.8}Cs_{0.2}Pb_{0.5}Sn_{0.5}I_3$ photodetector (Fig. S8b). The *EQE* profile is directly measured using the Enlitech QE-M110 system, while the photoresponsivity can be calculated according to the following equation:

$$R = EQE \times \lambda/1240 \quad (4)$$

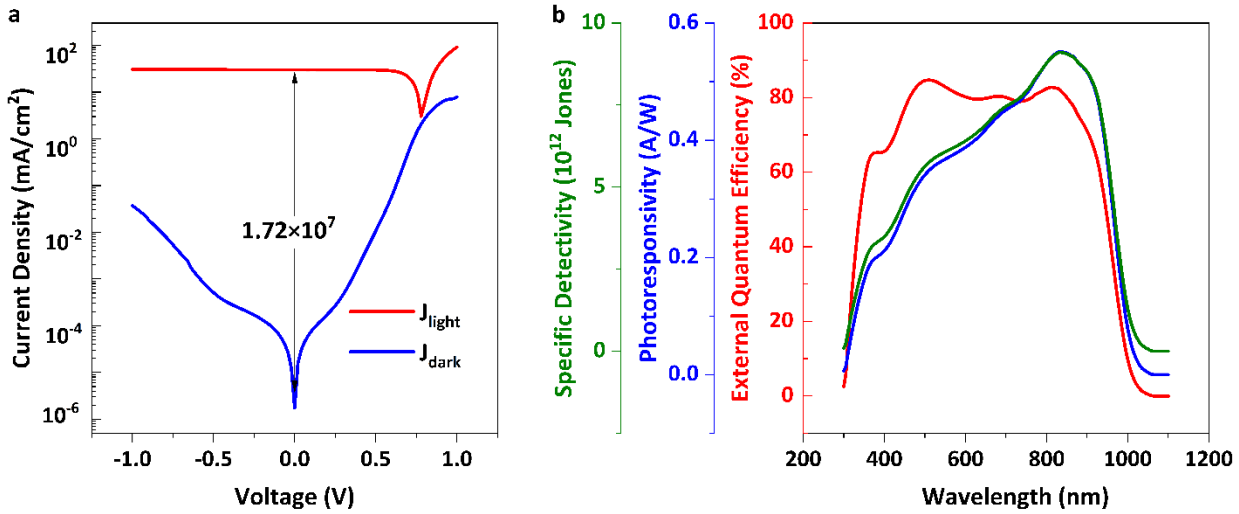

Fig. S8. Photodetecting performances of the perovskite photodetectors. (a) J-V characteristics recorded in dark and under AM 1.5G illumination (100 mW/cm^2), and (b) external quantum efficiency, photoresponsivity and specific detectivity profiles of the 800 nm $FA_{0.8}Cs_{0.2}Pb_{0.5}Sn_{0.5}I_3$ photodetectors, respectively.

where λ is the incident light wavelength. The specific detectivity (D^*) is then derived as

$$D^* = R \times (AB)^{1/2}/I_{noise} \quad (5)$$

where A represents the photodetecting area of the device, B is the noise measurement bandwidth, and I_{noise} is the total noise current of the device. Generally, the noise current is mainly composed of thermal noise, shot noise and flicker (1/f) noise, whereas the 1/f noise could be usually neglected in organic and perovskite-based diode-like photodetectors. Therefore, the noise current can be expressed as

$$I_{noise} = (I_{thermal}^2 + I_{shot}^2)^{1/2} = (4kTB/R_{shunt} + 2eI_dB)^{1/2} \quad (6)$$

while the specific detectivity (D^*) is derived accordingly

$$D^* = R \times A^{1/2}/(4kT/R_{shunt} + 2eI_d)^{1/2} \quad (7)$$

Note that the R maximum of the $FA_{0.8}Cs_{0.2}Pb_{0.5}Sn_{0.5}I_3$ photodetector reaches 0.56 A/W at 830 nm and remains 0.52 A/W at 900 nm, which is comparable to that of the silicon photodetectors (*47*). With the suppressed dark (noise) current and improved photoresponsivity, the specific detectivity (D^*) of the perovskite device is further enhanced. As shown in Fig. S8b, the present perovskite photodetector exhibits a high detectivity over 10^{12} Jones in the wide VIS-NIR range, ensuring the outstanding detection ability to weak light for night-vision sensing and imaging.

The capability of maintaining high specific detectivity under different incident light intensities, namely large linear dynamic range (LDR), is another critical factor for preciously perceiving and capturing shadowed images in complex environments. LDR is defined by the equation

$$LDR = 20 \times log(J_{max}/J_{min}) \quad (8)$$

where J_{max} and J_{min} are maximum and minimum photocurrent densities of the device recorded in the linear response region of the photocurrent density versus irradiation power curve. As shown in **Fig. 2f**, the photocurrents of the $FA_{0.8}Cs_{0.2}Pb_{0.5}Sn_{0.5}I_3$ device display a linear relationship with the white light irradiation intensity ranging from 0.1 W/cm^2 to 4×10^{-10} W/cm^2. It affords an LDR of 168 dB that is apparently greater than that of the Si photodetector (70 dB), InGaAs photodetector (66 dB), and two-dimensional material-based photodetectors (no more than 120 dB) (*48-52*). Note that the photoresponsivities of most existing retina-inspired sensor devices, although not reported, will most likely lag that of the present $FA_{0.8}Cs_{0.2}Pb_{0.5}Sn_{0.5}I_3$ photodetector.

Transient photocurrent of the perovskite photodetector was further measured with a nanosecond pulsed laser to evaluate its responding speed. The rising and falling times, when the photocurrents transit from 10% to 90% and 90% to 10% of the maximum value, respectively, are recorded as fast as 2.75 ns and 102.5 ns (Fig. S9a). In order to better understand the high performance of 800 nm $FA_{0.8}Cs_{0.2}Pb_{0.5}Sn_{0.5}I_3$ photodetector, transient photovoltage (TPV) decay curve was measured to gain insights into the charge recombination processes. As plotted in Fig. S9b, a doubled exponential photovoltage decay is observed, confirming that bulk phase rather than interface process dominates the charge carrier recombination (*53, 54*). Curve fitting reveals that the charge recombination lifetime (read at 1/e of the difference between the maximum and minimum photovoltages) of the present device is 2.45 μs, which is one of the longest carrier recombination lifetimes reported for Sn-Pb based NBG perovskite (*55, 56*). It corresponds to effective suppression of non-radiative recombination, which can improve the overall performance of photodetector devices. On the other hand, hole transport-only device with the configuration of ITO/PEDOT:PSS/perovskite/MoO_3/Au was also fabricated. As shown in Fig. S10, the dark J-V curve of this device displays a linear Ohmic response at low voltage range and a nonlinear rapid current increase in the high voltage stage where all defect states have been filled. According to the following equation:

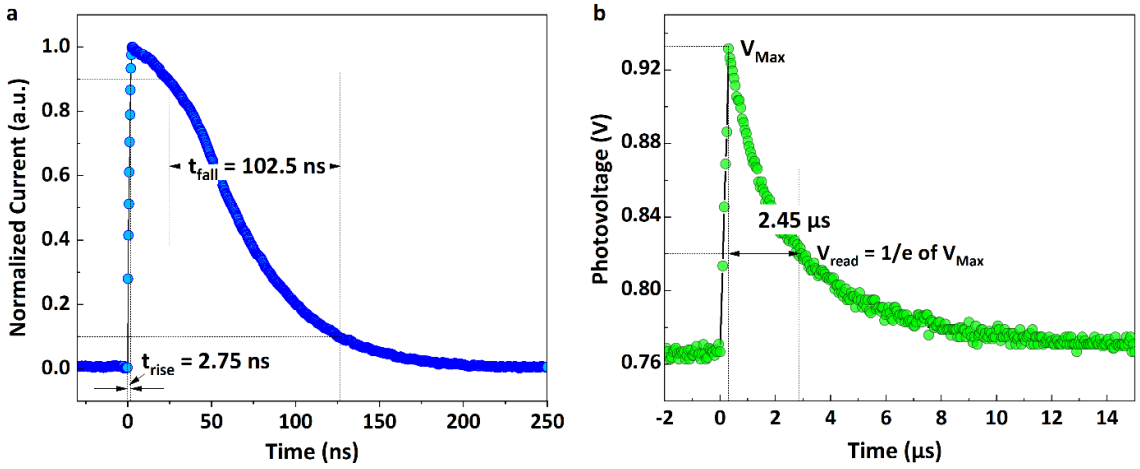

Fig. S9. Response time and charge recombination measurements. (a) TPC and (b) TPV curves of the $FA_{0.8}Cs_{0.2}Pb_{0.5}Sn_{0.5}I_3$ photodetector.

$$N_t = 2\varepsilon\varepsilon_0 V_{TFL}/eL^2 \quad (9)$$

where ε (51) is the relative dielectric constant of NBG perovskite (*57*), ε_0 (8.854×10^{-12} F/m) is the vacuum permittivity, V_{TFL} is the trap filled limit voltage (0.339 V, as read at the turning point), e is the elementary charge of an electron, and L is the thickness of the perovskite layer (800 nm), a low trap density of 2.98×10^{-15} cm^{-3} for the $FA_{0.8}Cs_{0.2}Pb_{0.5}Sn_{0.5}I_3$ photodetector can be estimated. It is smaller than most reported BNG perovskite devices (*9,10*), again confirming the high crystallinity quality of the as-prepared perovskite film for high-performance photodetecting applications.

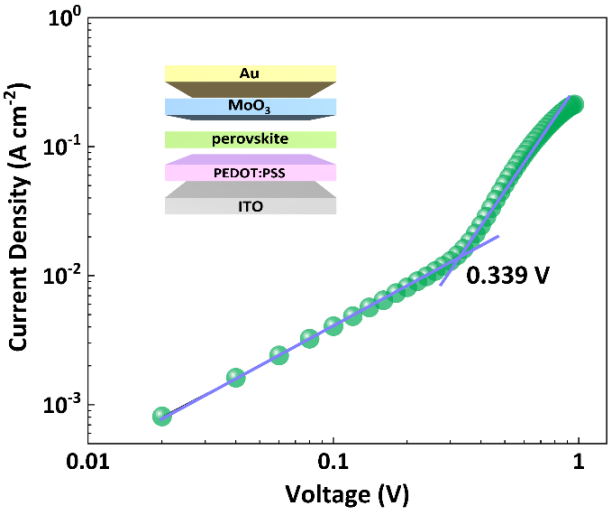

Fig. S10. Trap density estimation. J-V curve of the hole-only $FA_{0.8}Cs_{0.2}Pb_{0.5}Sn_{0.5}I_3$ photodetector. Inset shows device structure of ITO/PEDOT:PSS/perovskite/MoO_3/Au for trap density measurement conducted in dark condition.

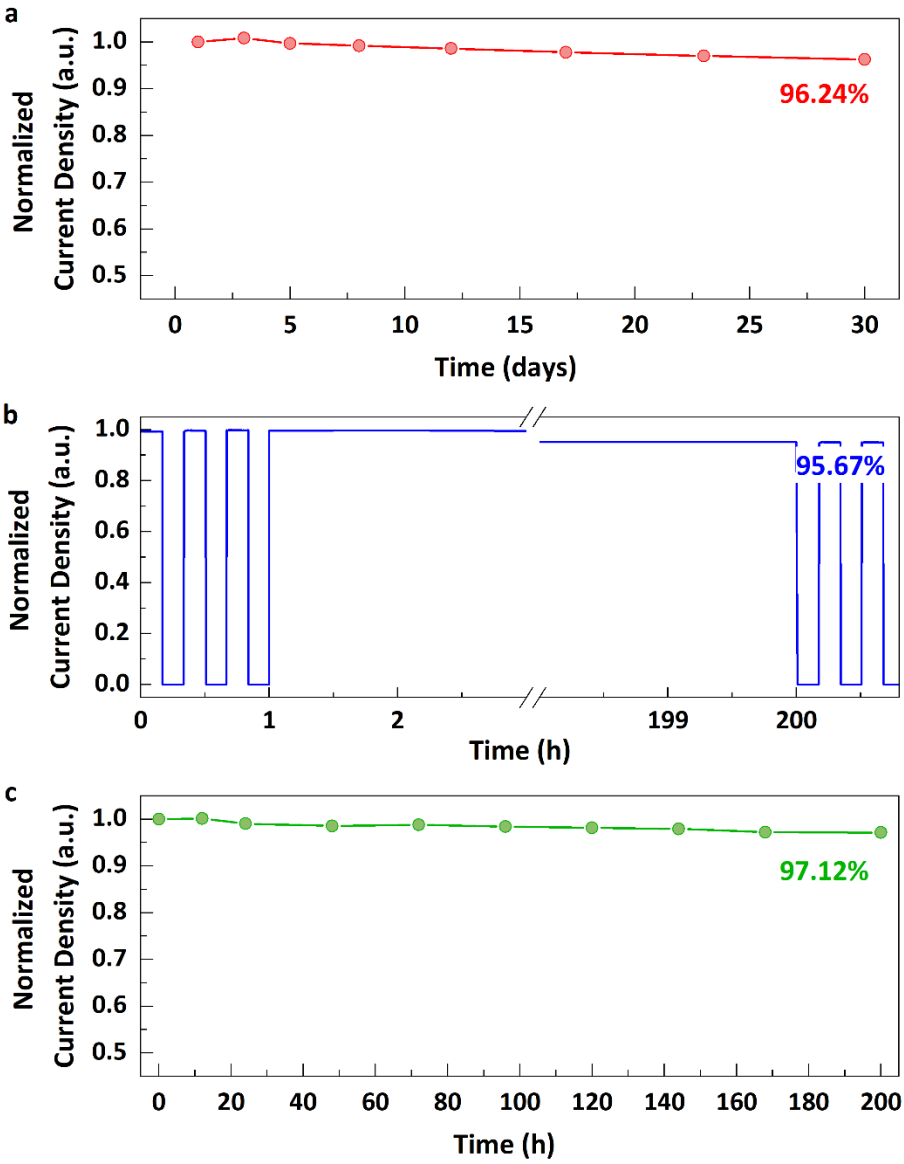

Fig. S11. Device stability of the perovskite photodetectors. Long-term photocurrent stability of the encapsulated $FA_{0.8}Cs_{0.2}Pb_{0.5}Sn_{0.5}I_3$ perovskite photodetector recorded (a) after 30 days, (b) after 200-hour continuous AM 1.5 G illumination and (c) after 200-hour heating at 80 ℃.

Considering the operation of the perovskite photodetectors in ambient environments, enhancing the long-time stability through proper encapsulation is essential. As summarized in Fig. S11, the optical sensing capability of the $FA_{0.8}Cs_{0.2}Pb_{0.5}Sn_{0.5}I_3$ device encapsulated with UV curing adhesive and glass slide can be retained for 96.24% after 30 days (a) and maintained as 95.67% after 200-hour continuous AM 1.5 G illumination (b), as well as retained as 97.12% after 200-hour heating at 80 ℃ (c).

4. Reconfiguration of photoresponsivity through ion migration in perovskite photodetector

To confirm the broadband photovoltaic response under VIS-NIR irradiation, the current density-voltage curves of the ITO/PEDOT:PSS/$FA_{0.8}Cs_{0.2}Pb_{0.5}Sn_{0.5}I_3$/$C_{60}$/BCP/Au device with circular top Au electrode of 100 μm diameter was measured at the wavelengths of 460 nm, 530 nm, 640 nm, 860 nm and 940 nm, respectively, with the irradiation power of 8 mW/cm^2. As plotted in Fig. S12a, open-circuit voltages of 0.33 V, 0.40 V, 0.48 V, 0.54 V and 0.44 V are observed under the respective blue, green, red, NIR-I and NIR-II monochromatic illuminations. Intriguingly, using the following equation

$$R = (J_{light} - J_{dark})/P_{in} \quad (10)$$

where J_{light} and J_{dark} are the photocurrent and dark current, P_{in} is the intensity of the monochromatic illumination, the photoresponsivities (R) read at 0 V are 0.34 A/W, 0.49 A/W, 0.86 A/W, 1.12 A/W and 0.73 A/W, respectively (Fig. S12b). Note that the broadband photovoltaic responses, as well as following measurements of the ITO/PEDOT:PSS/$FA_{0.8}Cs_{0.2}Pb_{0.5}Sn_{0.5}I_3$/$C_{60}$/BCP/Au device were recorded under optical illumination from the gold electrode side. The enhanced interaction between incident light and Au electrode layer through local surface plasmon resonance (LSPR) phenomenon will significantly improve the efficiency of optical absorption (*58*), resulting in ~ 200% increase in the photoresponsivity of the perovskite devices.

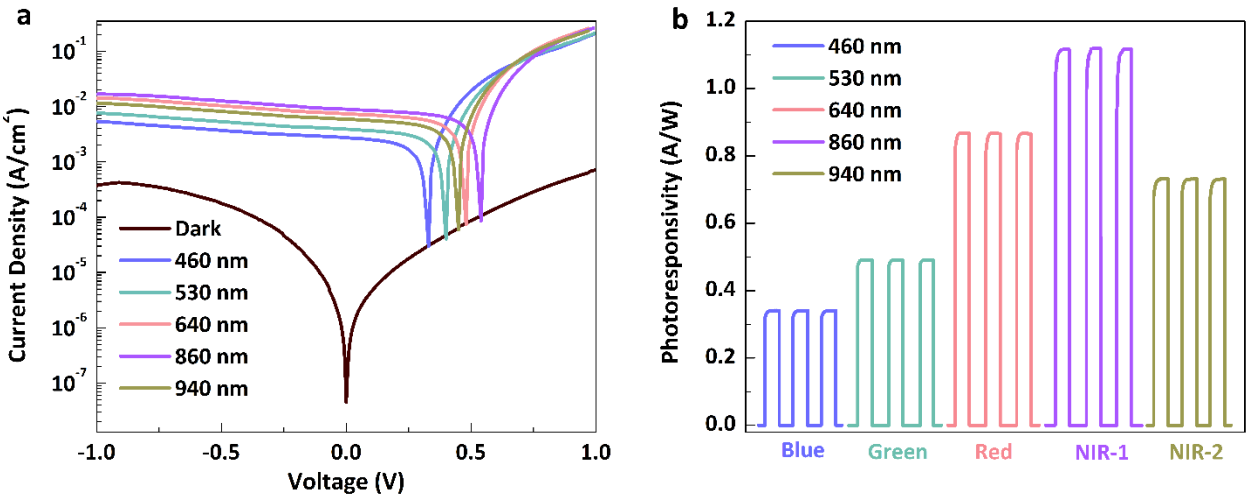

Fig. S12. Photoresponse performance. (a) J-V characteristics and (b) photoresponsivities of the $FA_{0.8}Cs_{0.2}Pb_{0.5}Sn_{0.5}I_3$ device recorded under visible light (RGB) and NIR light with the power density of 8 mW/cm^2.

In order to evaluate the consecutive and linear modulation capability of the $FA_{0.8}Cs_{0.2}Pb_{0.5}Sn_{0.5}I_3$ device photoresponsivity, a train of voltage pulses with the amplitude starting from 0 V, ramping step of -0.05 V and duration of 5 s was applied onto the photodetector through the Au top electrode. Again, the bottom ITO electrode was grounded during measurements. Under the monochromatic illumination of 8 mW/cm^2 at 860 nm, the perovskite device exhibits an initial photoresponsivity of 1.31 A/W. When voltage pulses with the ramping step of -0.05 V are applied, the photoresponsivity of the photodetector decreases continuously (Fig. S13). Curve fitting reveals that modulation of the device's photoresponsivity is monotonous and linear following the expression of

Resp=1.3211-0.01293×N, where N is the number of the modulation steps. The modulation rate and linearity are -1.29×10^{-2} A/W per step and 0.9981, respectively. In 32 steps the photoresponsivity of the perovskite devices is reduced to 0.92 A/W. Under the monochromatic illuminations of the same 8 mW/cm^2 intensity but different wavelengths of 940 nm, 640 nm, 530 nm and 460 nm, similar monotonous and linear modulation characteristics are also demonstrated for the $FA_{0.8}Cs_{0.2}Pb_{0.5}Sn_{0.5}I_3$ photodetector (Fig. S13 and Table S1). Moreover, the slope values of are -0.00507, -0.00635, -0.00880, -0.01293 and -0.00783 A/W for the perovskite devices under light illumination with the wavelengths of 460, 530, 640, 860 and 940 nm, indicating different modulation degree at these wavelengths. Noted that the initial photoresponsivities of 0.45, 0.66, 0.98, 1.31 and 0.91 A/W are observed under the respective monochromatic illuminations. Higher photoresponsivity suggests that more carriers including electron and hole are generated and transferred to the corresponding transporting layers. The higher photogenerated carrier density can reduce the activation energy for ion migration within perovskite and facilitates the migration of cations and anions, respectively (*59, 60*). Thus, the accelerated ion migration behaviors would increase the modulation degree of perovskite devices. Note that high ON/OFF ratio exceeding 9×10^3 can be well maintained after photoresponsivity reconfiguration by ion migration process, which again guarantees excellent image sensing operation with large contrast in dim-light environments.

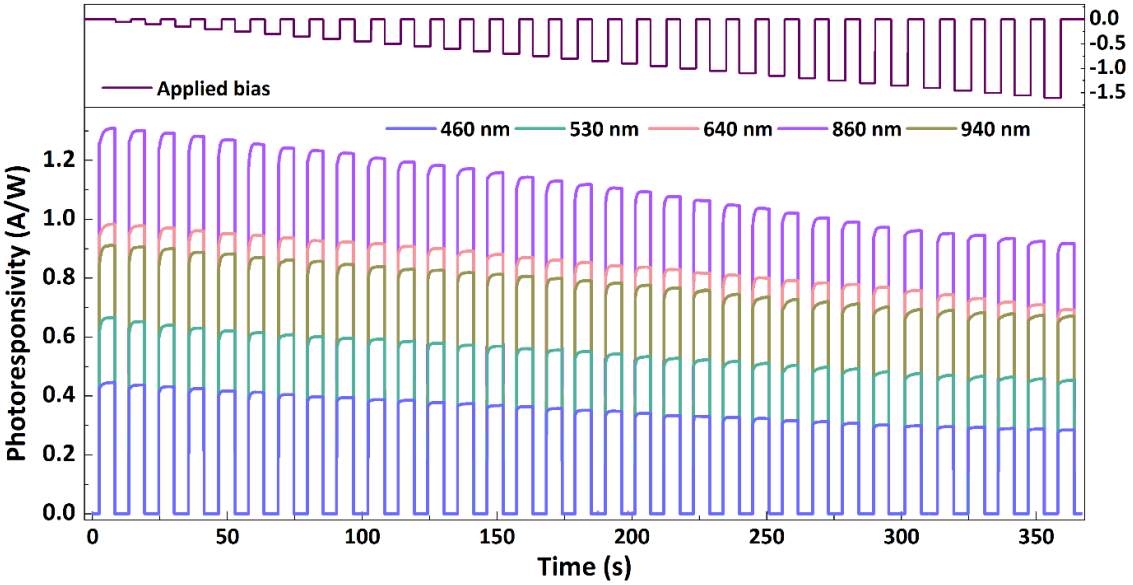

Fig. S13. Linear modulation of broadband photoresponsivity. Linear modulation of photoresponsivity of the $FA_{0.8}Cs_{0.2}Pb_{0.5}Sn_{0.5}I_3$ device under light illumination at the wavelengths of 460, 530, 640, 860 and 940 nm by voltage stimuli.

To further confirm the favorable stability and reliability, the device performance of reconfigurable perovskite photodetector after long-term cycles are measured. As shown in Fig. S14, the photoresponsivity of perovskite photodetector exhibits strong consistency even after 10000 cycles without any significant fluctuations. Moreover, the consecutive and linear modulation of perovskite device photoresponsivity are evaluated after 10000 cycles. Under the monochromatic 860

Table S1. Linear modulation of photoresponsivity. The linear fitting function and linearity of perovskite device under VIS-NIR light illumination.

Wavelength (nm)	R_0 (A/W)	R_1 (A/W)	Linear fitting function	R^2
460	0.4464	0.2846	$Resp=0.4365-0.00507\times N$	0.9920
530	0.6648	0.4540	$Resp=0.6511-0.00635\times N$	0.9958
640	0.9842	0.6927	$Resp=0.9917-0.00880\times N$	0.9956
860	1.3130	0.9176	$Resp=1.3211-0.01293\times N$	0.9981
940	0.9100	0.6714	$Resp=0.9124-0.00783\times N$	0.9973

R_0 and R_1 are the initial and final device photoresponsivities, *Resp* is the photoresponsivity, *N* is the number of the modulation steps and R^2 is the modulation linearity.

nm light illumination with same voltage pulses and ramping step, the device still maintains excellent modulation linearity of 0.9976 and the linear fitting function is fitted to be $Resp=1.2931-0.01332\times N$, which is similar to the initial function without long-term cycles ($Resp=1.3211-0.01293\times N$). The results demonstrated excellent reproducibility and stability of perovskite device for practical applications. Developing perovskite with different nanoscale morphology such as quantum dots, nanosheets, nanowires, and nanocrystals may further improve the device stability. Inserting buffer layers at the contact interface could also improve the sample stability by suppressing the chemical reactions between perovskite, charge transport layer, and metal electrode. Nevertheless, these attempts are beyond the scope of the present study.

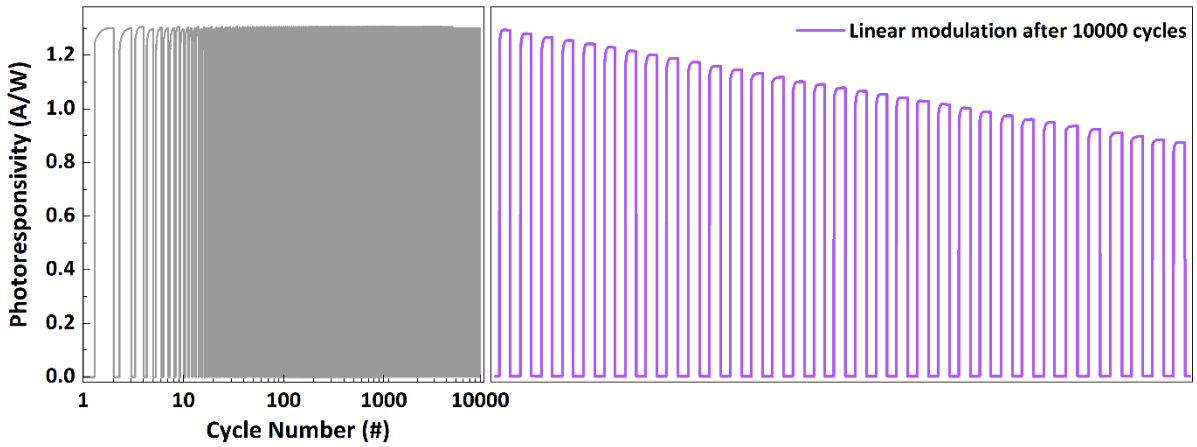

Fig. S14. Stability and reliability of the perovskite devices. Cycling stability of the perovskite device under the illumination of 860 nm light and the linear modulation of photoresponsivity after 10000 modulating cycles.

Coincident with the occurrence of giant switching in the photovoltaic characteristics induced by the ion migration phenomenon, evolution of the local photoconductances of the $FA_{0.8}Cs_{0.2}Pb_{0.5}Sn_{0.5}I_3$ thin film were also monitored by conductive-atomic force microscopic measurement. Herein, the perovskite layer was deposited directly on ITO substrate using the same recipe for full-structure photodetector. During C-AFM measurements, a conducting cantilever coated with Pt was used as a movable electrode to form the Pt/perovskite/ITO structure. The voltage biases were applied with the Pt cantilever tip to induce ion migration and record the local photocurrents under white light illumination of 8 mW/cm^2. Photoconductances are then calculated by dividing the recorded photocurrent values by the amplitudes of the applied voltage. As shown in Fig. S15, the 5×5 μm^2 pristine perovskite film displays low photoconductance of 10^{-3} pS under zero bias. When a positive voltage bias of 1.0 V is applied to induce iodine anion migration towards the top Au electrode, the photoconductance increases locally over the perovskite layer. This is in good agreement with the localized occurrence of ion migration in perovskite device. As the amplitudes of the positive voltage bias increases to 2.0 V, the photoconductance of the entirely perovskite film increases significantly to 3.08±0.68 pS. When negative voltage is applied through the ITO substrate with decreasing amplitudes from -2.0 V to -1.0 V, back migration of the iodine anions to their initial position and therefore recovery of device energy band diagram occurs. As a result, the photoconductances of the Pt/perovskite/ITO structure consecutively decrease and return to the initial value when the biased voltage drops to 0 V. Both the dc sweeps of the macroscopic full-structure $FA_{0.8}Cs_{0.2}Pb_{0.5}Sn_{0.5}I_3$ photodetectors and the microscopic C-AFM measurements confirm that the photoresponses of the perovskite layer can be reconfigured controllably by ion migration phenomena.

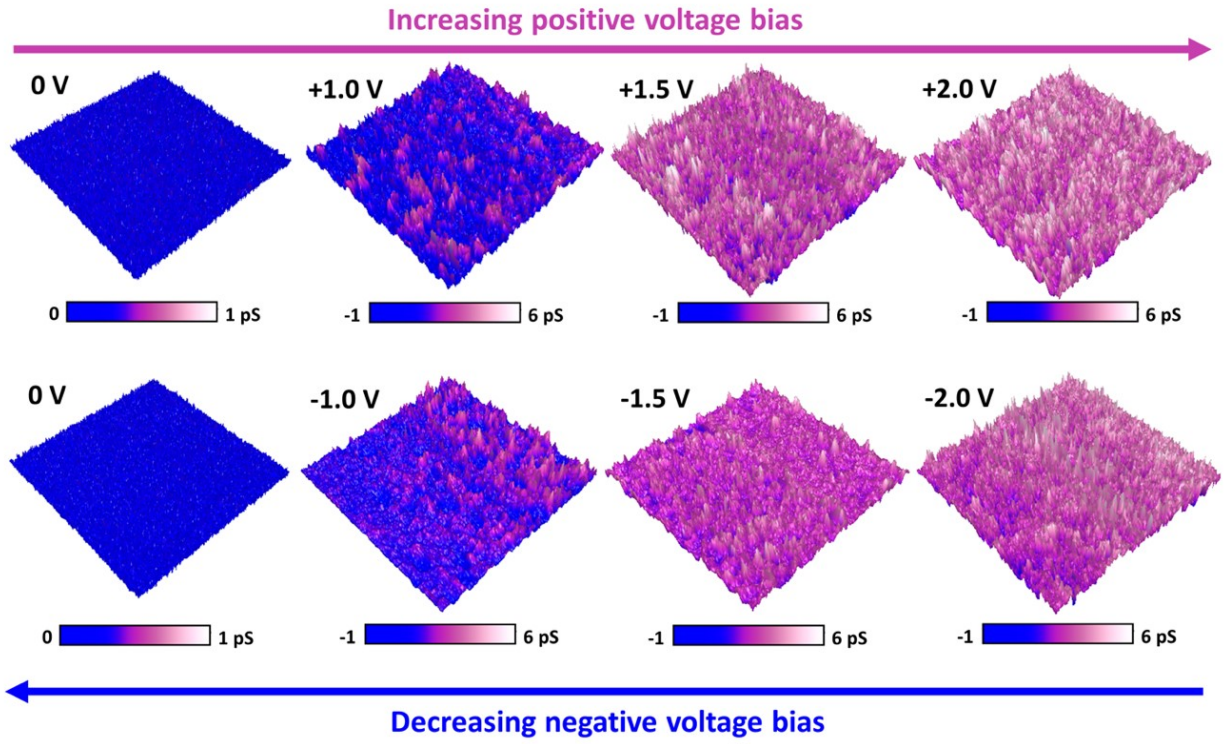

Fig. S15. C-AFM measurements. Photoconductance evolution of the $FA_{0.8}Cs_{0.2}Pb_{0.5}Sn_{0.5}I_3$ device under biased voltages.

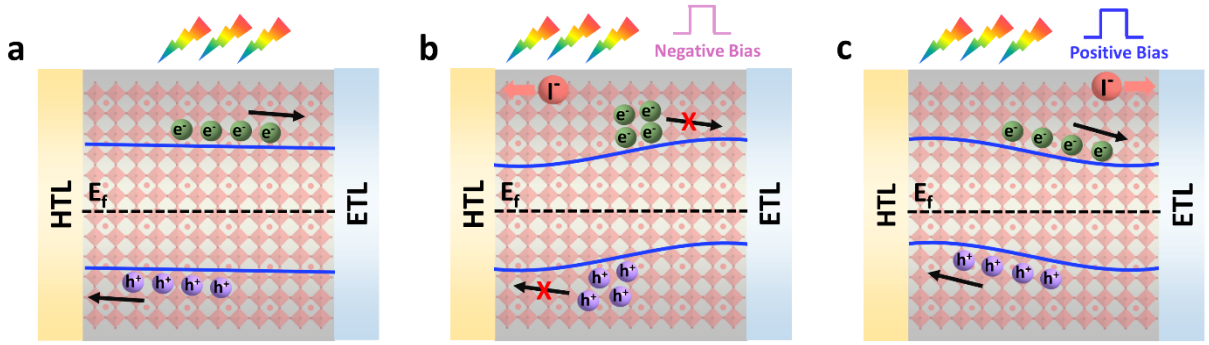

Fig. S16. Schematic diagrams of energy band. (a) Pristine state, and under (b) negative and (c) positive voltage biases applied on the Au electrode.

When perovskite is subjected to external voltage bias, the mobile ions will migrate considerably, which provides exotic opportunity of photoresponsivity reconfiguration through modulation of material's composition and device energy band diagram. When external voltage is not applied (Fig. S16a), the perovskite device works as a traditional solar cell. Upon optical irradiation, excitons are generated and dissociated into free charge carriers (electrons and holes) along with the energy offset. Then, they are significantly transported to the respective electron transporting layer (ETL) and hole transporting layer (HTL), and collected by electrode to generate the photocurrent and photovoltage. Migration of ion such as iodine anions under the influence of an electric field would change the charge transfer and collection process to manipulate the device photoresponsivity. When applying a negative voltage on the Au electrode, the iodine anions migrate to the HTL/ITO side correspondingly. The energy band bends downward and screen the charge transfer towards the charge-selective interfaces (Fig. S16b), thereby decreasing the photogenerated current and photoresponsivity of photodetectors. As for the condition of applying positive external voltage, the iodine anions migrate reversely to the ETL/Au side. Consequently, the energy band bends upward and promotes the charge transfer that increase the device photoresponsivity (Fig. S16c). Thus, the reversible applied voltage would affect the energy band of perovskite device and effectively reconfigure the photoresponsivity.

5. Optoelectronic performance of 4096-pixel 1T-1PD retinomorphic sensor array

Fig. S17 displays the circuit structure of the perovskite-based RSA, wherein the 4096 1T-1PD pixels are arranged in a 64 row × 64 column architecture. In each pixel the bottom electrode of the photodetector is connected to the drain electrode of the amorphous silicon transistor, while the gate and source electrodes of the TFTs are connected in row-wise (select lines) and column-wise (operate lines) manner, respectively. The top electrodes of all the photodetectors are connected to a common terminal. Through applying biases that exceed the TFT's threshold voltage to the m^{th} selector line, the stressed transistors will be turned ON to enable selection of the photodetectors in that particular row. Then the application of voltage stimuli to the n^{th} operation line will allow either photoresponsivity modulation or photocurrent readout of the photodetector in the m^{th} row and n^{th} column of the 4096-pixel sensor array, depending on the amplitude of the applied voltage stimuli.

Fig. S18a shows that at V_{DS}=-1 V, the OFF-state dark current and resistance of the 1T-1PD cell based on amorphous silicon thin film transistor and $FA_{0.8}Cs_{0.2}Pb_{0.5}Sn_{0.5}I_3$ photodetector are 5.99×10^{-9} A and 1.67×10^{8} Ω, respectively. When V_G=10 V is applied, the corresponding dark current and pixel resistance become 1.33×10^{-7} A and 7.52×10^{6} Ω. Note that the α-Si TFT has an ON/OFF ratio of 2.74×10^{4} at V_{DS}=-1 V, the resistances of the transistor (A) and photodetector (B) devices read at V_G=10 V are roughly estimated as 5.82×10^{3} Ω and 7.51×10^{6} Ω, according to the following expression

$$2.74 \times 10^4 \times A + B = 8.14 \times 10^8\ \Omega \tag{11}$$

$$A + B = 6.24 \times 10^6\ \Omega \tag{12}$$

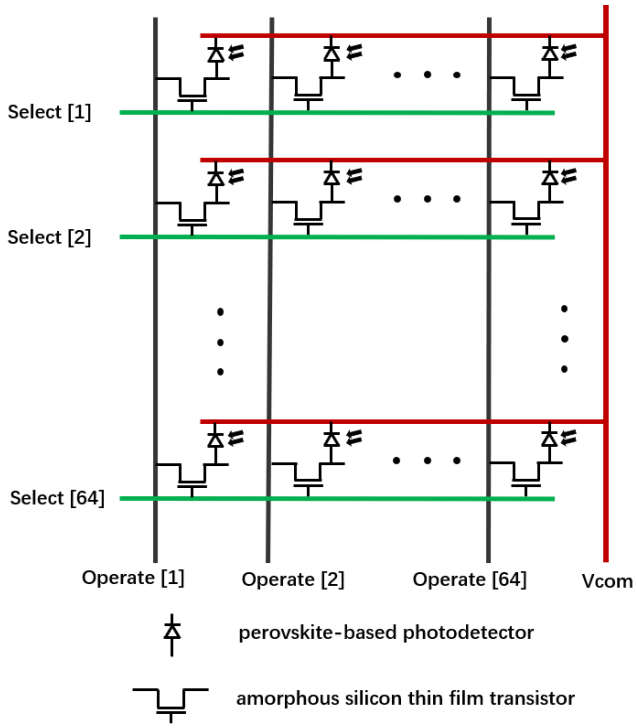

Fig. S17. Circuit structure. Circuit layout of the 4096-pixel 1T-1PD retinomorphic image sensor array.

while the OFF-state resistance of the transistor is $5.82\times10^3\times2.74\times10^4=1.60\times10^8$ Ω. In case that a certain pixel is not selected by turning ON the transistor, the resistance of its TFT (1.60×10^8 Ω) is more than 21 times of that of its perovskite photodetector (7.51×10^6 Ω). Thus, majority part of the V_{DS} applied onto pixel will fall on the transistor device. Without sufficient share of the V_{DS} as driving force to induce ion migration in the perovskite layer, the photoresponsivity of the detector device will not be modulated. When V_G exceeding the threshold voltage of the α-Si transistor is applied to select the pixel, the TFT is turned on with its resistance decreasing to 5.82×10^3 Ω. It is 1290 times smaller than that of the perovskite photodetector, and sufficient share of the V_{DS} will drop onto the perovskite device to induce ion migration and photoresponsivity modulation. For source-drain voltages of -0.1 V and -10 V, similar selection and photoresponsivity modulation operations will be allowed for the 1T-1PD cell. The transfer curves of the 1T-1PD pixel recorded under the monochromatic illuminations at the wavelengths of 940 nm, 860 nm, 640 nm, 530 nm and 460 nm, with the optical power of 8 mW/cm^2 and the source-drain voltage of 1 V are summarized in Fig. S18b.

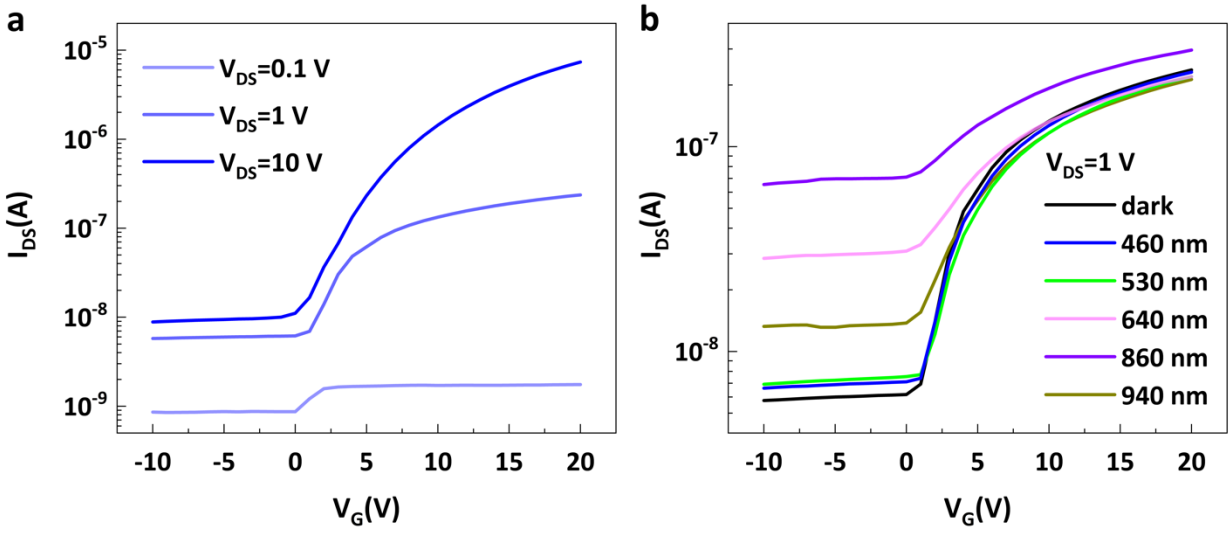

Fig. S18. Optoelectronic performance of the 1T-1PD cell. Transfer curves recorded (a) in dark conditions at V_{DS}=0.1 V, 1 V and 10 V, respectively and (b) under monochromatic illumination at the wavelengths of 940 nm, 860 nm, 640 nm, 530 nm and 460 nm with the optical power of 8 mW/cm^2 and V_{DS}=1 V.

Table S2. Photoresponsivity modulation of 1T-1PD cell. Linear and reversible modulation of photoresponsivity.

Wavelength (nm)	Linear fitting function of inhibitory modulation		R^2	Linear fitting function of excitory modulation		R^2
460	*Dec*	*Resp*=16.46-0.894×*N*	0.9967	*Inc*	*Resp*=17.23+1.255×*N*	0.9989
	Inc	*Resp*=2.329+0.935×*N*	0.9966	*Dec*	*Resp*=35.83-1.276×*N*	0.9906

530	*Dec*	*Resp*=19.25-1.035×*N*	0.9963	*Inc*	*Resp*=19.83+1.433×*N*	0.9979
	Inc	*Resp*=3.059+1.102×*N*	0.9952	*Dec*	*Resp*=42.50-1.529×*N*	0.9912
640	*Dec*	*Resp*=24.06-1.184×*N*	0.9972	*Inc*	*Resp*=25.22+1.660×*N*	0.9982
	Inc	*Resp*=5.202+1.264×*N*	0.9979	*Dec*	*Resp*=50.07-1.725×*N*	0.9914
860	*Dec*	*Resp*=27.23-1.355×*N*	0.9963	*Inc*	*Resp*=27.90+1.872×*N*	0.9988
	Inc	*Resp*=6.007+1.385×*N*	0.9948	*Dec*	*Resp*=55.68-1.916×*N*	0.9964
940	*Dec*	*Resp*=22.37-1.149×*N*	0.9969	*Inc*	*Resp*=23.07+1.556×*N*	0.9974
	Inc	*Resp*=4.494+1.168×*N*	0.9960	*Dec*	*Resp*=46.42-1.620×*N*	0.9907

Resp is the photoresponsivity, *N* is the state numbers and R^2 is the modulation linearity. Dec denotes "decreasing" while Inc stands for "increasing" of the device photoresponsivity.

6. Image sensing performance of 4096-pixel 1T-1PD retinomorphic sensor array

The 4096-pixel perovskite RSA with 1T-1PD structure was connected to a commercial readout circuit (Zill Box as provided by Linkzill) through a flexible printed cable (FPC). Both of the gate selecting voltage and source modulating/reading voltage can be varied in the range of -15 V to +15 V. The detected dark currents and photocurrents of the pixels are transmitted to mobile terminals through WIFI connection and displayed in both raw data and image modes.

As shown in Fig. S19a and Movie S1, the perovskite RSA is firstly covered with a black plastic shelter for dark current measurement. According to the following equation

$$Uniformity\ (\%) = (1 - {}^{\delta}/_{\mu}) \times 100\% \quad (13)$$

where δ and μ are the standard deviation and average value of the performance parameter, the RSA displays a high pixel-to-pixel uniformity (PPU) of 97.73% for the dark currents. Afterwards, the plastic shelter is removed and the fully-exposed photocurrents of the perovskite RSA pixels are recorded under white light illuminations of 0.01 mW/cm^2, 0.05 mW/cm^2, 0.10 mW/cm^2 and 0.20 mW/cm^2 with a commercial LED lamp (Fig. S19b). The light irradiations are introduced directly above the RSA. As shown in **Fig. 3b**, **3c** and S19c-19e, the RSA exhibits average photocurrents and PPUs of 11.84 nA/95.82%, 50.12 nA/96.22%, 91.47nA/97.15% and 181.37nA/ 97.85%, respectively. Note that the maximum photocurrent reading limit of Zill Box is 200 nA, the acquired photocurrent becomes saturated at the illumination intensity of 0.5 mA/cm^2 and source voltage of 0.1 V.

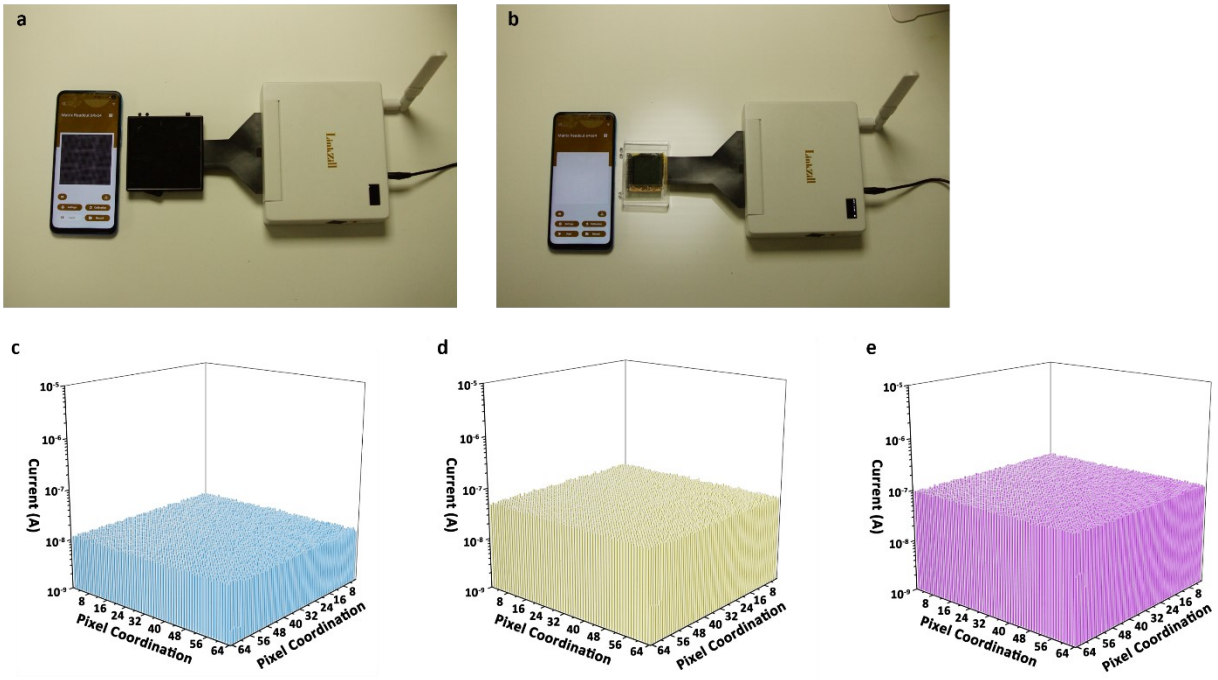

Fig. S19. Experimental setups and photocurrent mapping. Experimental setups for (a) dark and (b) photo current measurements of the perovskite RSA. Photocurrent mapping over the 4096 pixels of the RSA under white light illuminations of (c) 0.01 mW/cm^2, (d) 0.05 mW/cm^2 and (e) 0.10 mW/cm^2, respectively.

During image sensing experiments using the perovskite RSA, handwritten digits “2023” and letters “SJTU” are obtained from MNIST database and printed on transparent plastic sheets. These plastic sheets and entities of metallic paper clip, keyset and hairpin are placed directly on top of the RSA, with lights of various wavelengths and intensities illuminated from right top of the samples. As such, the pixels covered by the imaging samples will output dark currents, while the pixels being exposed to incident light will deliver relative high photocurrents. By collecting current responses of all pixels, images of the sensing samples will be reconstructed and displayed by the Zill Box and software on the mobile terminal (Movie S2).

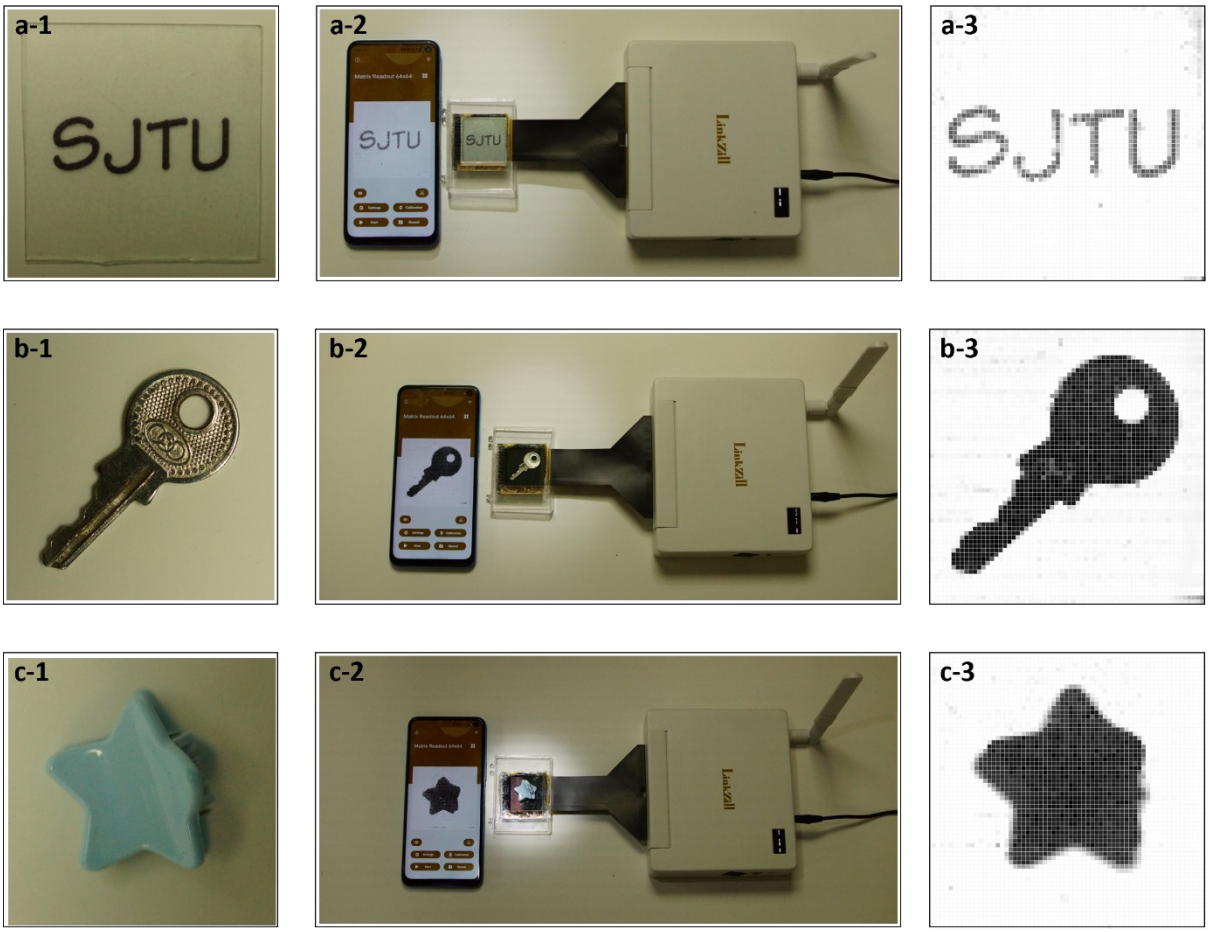

Fig. S20. Image sensing experiments. Photographs, experimental imaging setups with the perovskite RSA (V_{DS}=0.1 V, V_G=10 V) and captured images of the (a) handwritten letters, (b) key and (c) hairpin under white light illumination of 0.2 mW/cm^2.

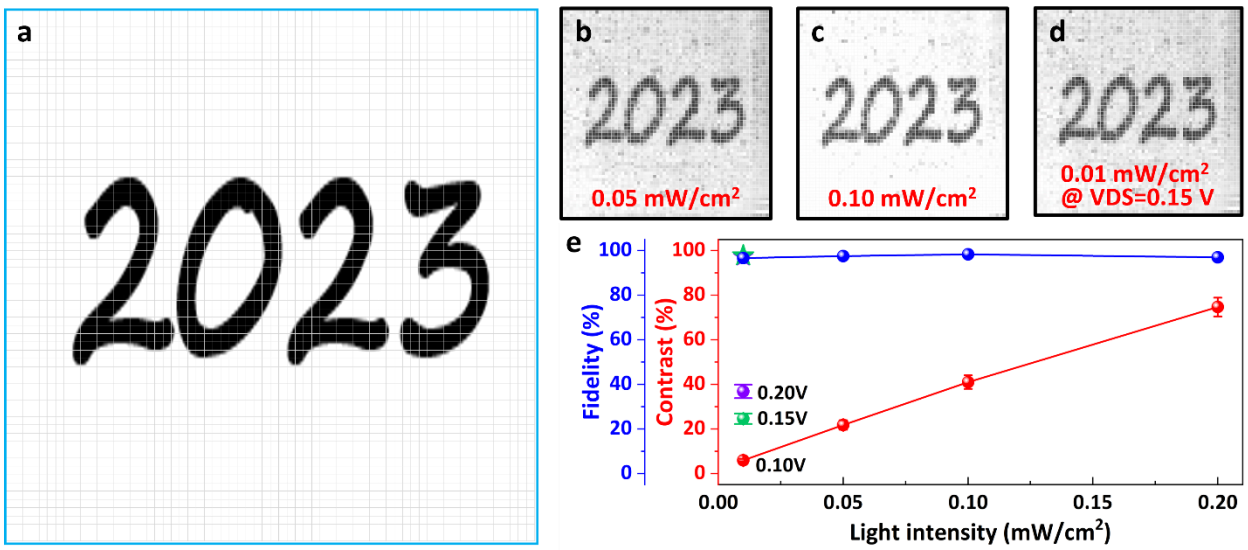

Fig. S21. Adaptive image sensing performance. (a) Zoom-in view of handwritten digits "2023", as well as images acquired under white light illuminations of (b) 0.05 mW/cm^2 and (c) 0.10 mW/cm^2, respectively. (d) displays the image of handwritten digits acquired under 0.01 mW/cm^2 illumination, upon photoresponsivity amplification by source modulation voltage of 0.15 V. (e) shows the contrasts and fidelities of the images acquired under various illumination intensities, without and with photoresponsivity amplification by 0.15 V and 0.20 V source voltage.

Fig. S21a shows a zoom-in view of the handwritten digits "2023" printed on the plastic sheet. It occupies 505 pixels in the original template. Under illumination of 0.01 mW/cm^2, handwritten digits "2023" occupy 488 pixels in the acquired image. The image sensing fidelity of the perovskite RSA is thus calculated as 488/505×100% =96.63% in dim light environment. As shown in Fig. S22, similar fidelities are also recorded under the other optical illumination intensities.

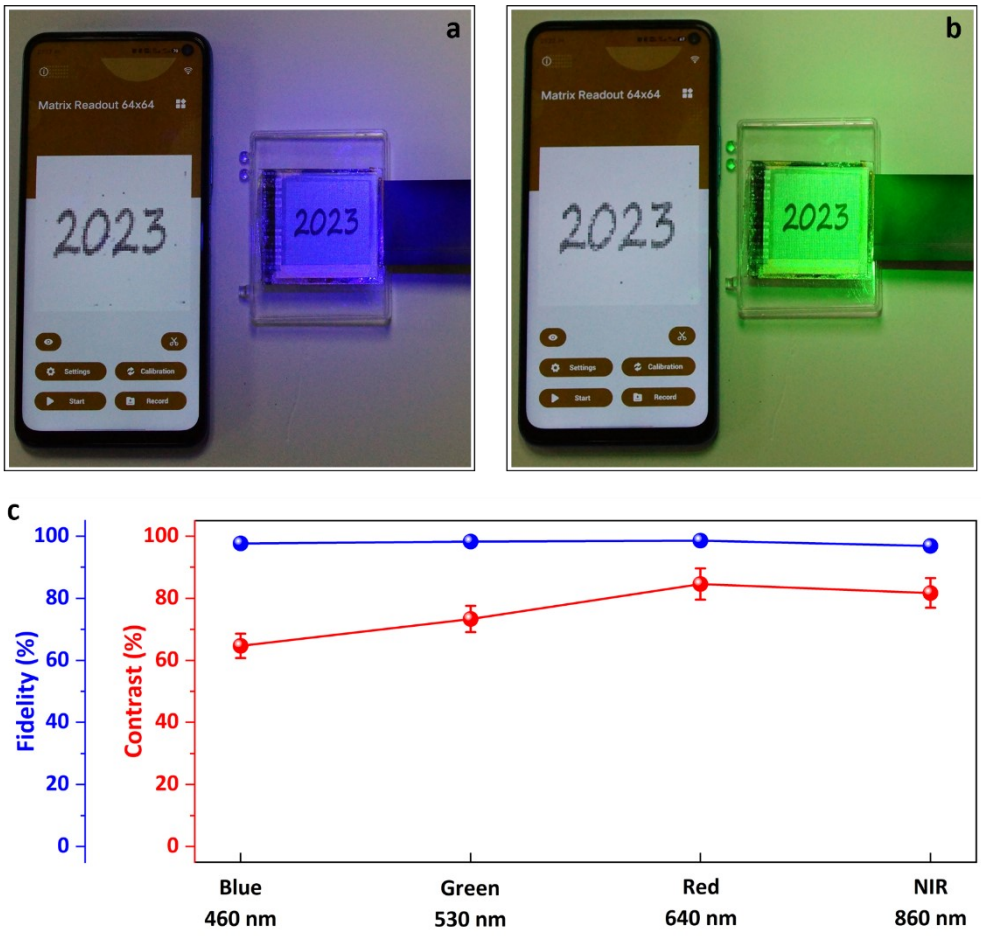

Fig. S22. Image sensing performance under different light illumination. Images of the hand-written digits "2023" acquired under 0.2 mW/cm^2 monochromic illuminations at the wavelengths of (a) 460 nm and (b) 530 nm, respectively. (c) displays the contrasts and fidelities of the acquired images captured under monochromic illuminations of different wavelengths.

7. Retinomorphic computing with 4096-pixel 1T-1PD retinomorphic sensor array

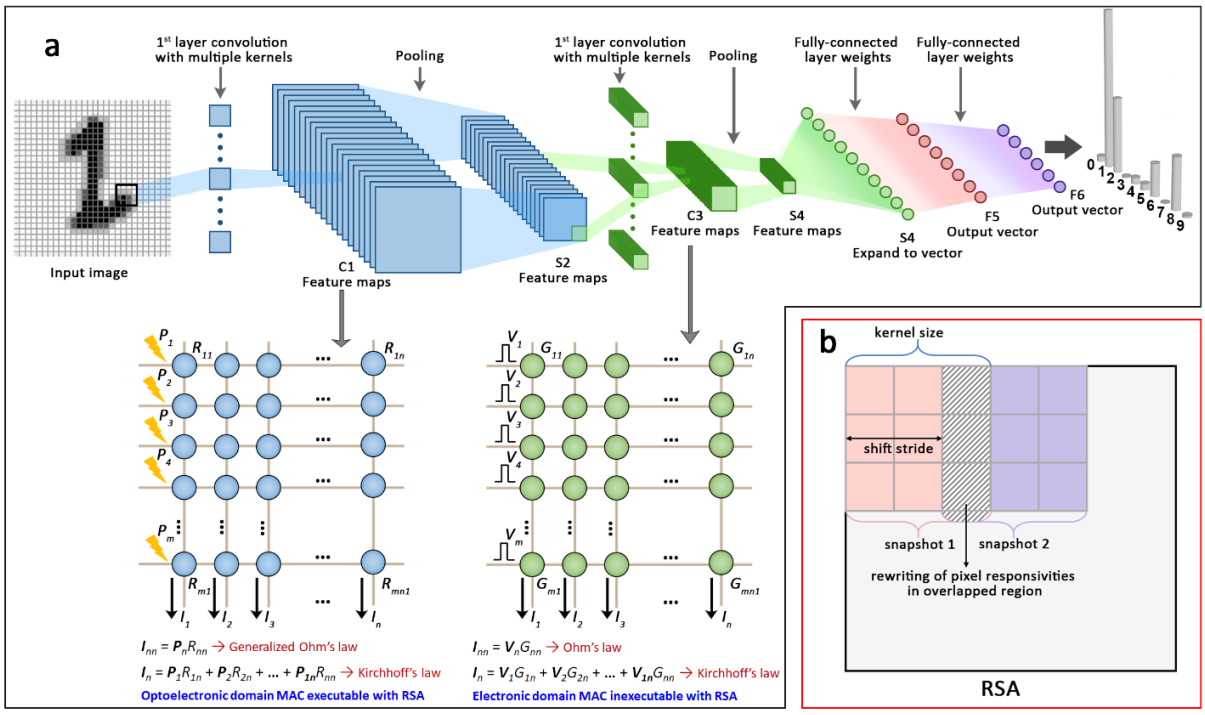

Fig. S23. Schematic illustration of convolution neural network. (a) Schematic illustration of multilayer convolution neural network using multiple kernels and execution of the first layer convolution *via* optoelectronic MAC operations in the retinomorphic sensor array. (b) Small-stride shifting of the convolution kernel that results in rewriting of pixel photoresponsivity and repeated image capturing during convolution.

Upon the execution of one-dimensional feature extraction on the perovskite RSA, the encoded information is taken as input of the fully-connected neural network layers. The forward propagation between these layers is divided into two parts: linear transformation of $Z^l=a^{l-1}\times W^l+b^l$ and nonlinear activation of $a^l=f(Z^l)$, where Z represents both output of the linear transformation and input of the nonlinear activation, a is output of the nonlinear activation and input of the next fully-connected layer, while f is the activation-rectified linear unit (ReLU) function and expressed as y=max (0, x). The fully connected layers consolidate spatial information from preceding feature-extraction operations with a FPGA-based digital circuit, enhancing pattern discernment and ensuring resilient classification outcomes.

As depicted in Fig. S24, the training of the FOPR-Net primarily involves initialization, forward propagation, and backward propagation. In the initialization process, the synaptic weights in the column vector *W* of the feature-extraction layer and fully-connected layers are set to random values. In the forward propagation process, samples in the training dataset are grouped into batches, with one batch fed into the network each time. As the batch fed in, the network computing forward propagates across the feature-extraction layer and following fully-connected layers. Subsequently,

the loss information representing the discrepancy between the predicted result of the FOPR-Net and the actual target label is calculated using the L2 loss Function. Finally, the calculated loss is

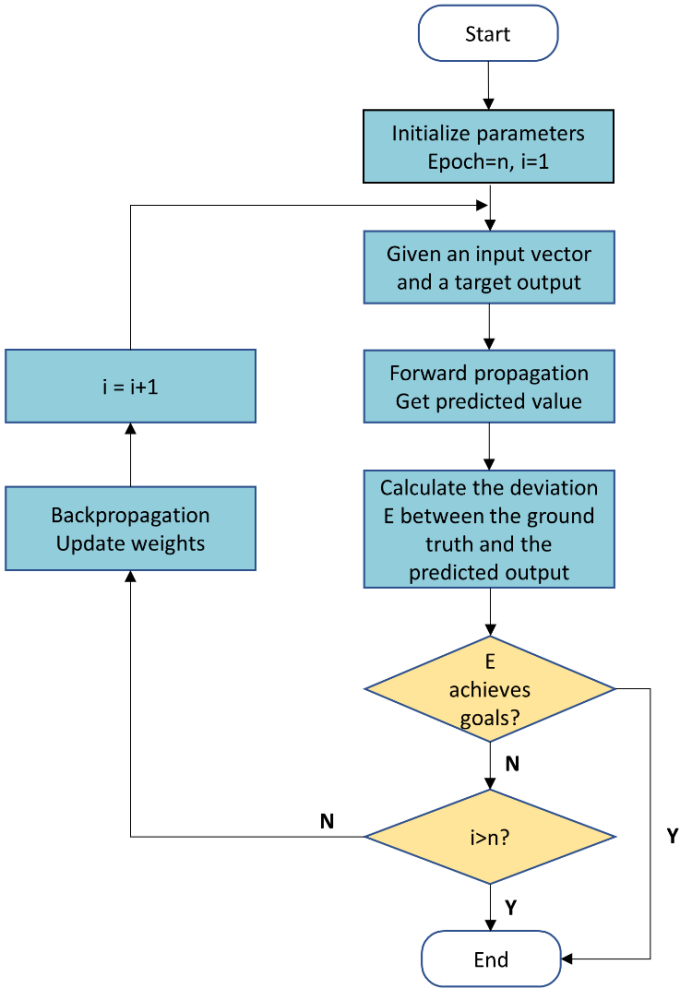

Fig. S24. Training process of the FOPR-Net. The process composed of a column-wise feature extraction layer and three fully-connected layers.

backpropagated from the output layer to each preceding layer of the network. Meanwhile, the gradients of the loss function with respect to each weight are calculated layer by layer according to the chain rule. The synaptic weights are updated with gradient descent technique, leading to necessary adjustment to minimize the loss function result. The forward and backward propagations are repeated iteratively with samples fed by batches. When all samples in the training dataset are used up, a single epoch completes. According to the probability number generated by the FOPR-Net for each of the 10 handwritten digits, the input handwritten image is classified into a certain category and compared with its pre-defined label. If the classified outcome coincides with the label, the network training ends successfully. Otherwise, the train process continues to improve the recognition accuracy of the network. The training accuracy is calculated as the ratio of numbers of the correctly recognized samples to that of the overall samples.

Table S3. Synaptic weight and photoresponsivity vectors. One-dimensional-vector pixel weights and photoresponsivities of the RSA upon 30-epoch FORP-Net training.

Pixel No.	Weight	Photoresponsivity (A/W)	Pixel No.	Weight	Photoresponsivity (A/W)
1	-0.06250	28.8845	33	-0.25000	24.2014
2	-0.06250	28.8845	34	-0.25000	24.2014
3	-0.12500	27.3777	35	-0.12500	27.3777
4	-0.06250	28.8845	36	-0.12500	27.3777
5	-0.12500	27.3777	37	-0.25000	24.2014
6	-0.12500	27.3777	38	0.00000	29.8618
7	0.00000	29.8618	39	-0.18750	25.8709
8	-0.06250	28.8845	40	-0.12500	27.3777
9	-0.1850	26.5120	41	-0.06250	28.8845
10	-0.25000	24.2014	42	-0.06250	28.8845
11	-0.37500	21.2694	43	-0.06250	28.8845
12	-0.43750	19.5183	44	-0.12500	27.3777
13	-0.31250	22.9389	45	-0.06250	28.8845
14	-0.37500	21.2694	46	-0.06250	28.8845
15	-0.37500	21.2694	47	-0.12500	27.3777
16	-0.31250	22.9389	48	-0.06250	28.8845
17	-0.37500	21.2694	49	-0.12500	27.3777
18	-0.37500	21.2694	50	-0.12500	27.3777
19	-0.25000	24.2014	51	0.00000	29.8618
20	-0.37250	21.6603	52	-0.18750	25.8709
21	-0.31250	22.9389	53	0.00000	29.8618
22	-0.37250	21.6603	54	-0.12500	27.3777
23	-0.43750	19.5183	55	-0.18750	25.8709
24	-0.37500	21.2694	56	-0.12500	27.3777
25	-0.31250	22.9389	57	0.12500	32.5495
26	-0.43750	19.5183	58	0.12500	32.5495
27	-0.37500	21.2694	59	0.31250	37.1511
28	-0.56250	16.6677	60	0.06250	31.5314
29	-0.56250	16.6677	61	0.06250	31.5314
30	-0.43750	19.5183	62	-0.12500	27.3777
31	-0.43750	19.5183	63	-0.12500	27.3777
32	-0.31250	22.9389	64	0.00000	29.8618

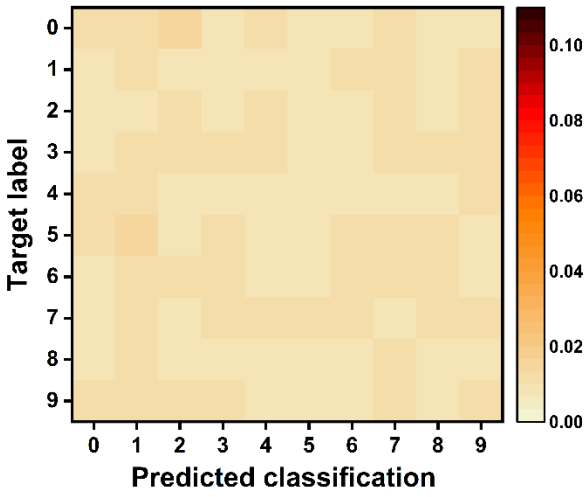

Fig. S25. Confusion matrices of the FOPR-Net summarized in the initial state.

Finally, we implement a retinomorphic computing hardware system consisting of a 4096-pixel perovskite-based RSA, a home-made printed circuit board (PCB) to drive and read the RSA pixel data, and a commercial Xilinx Zynq UltraScale+MPSOC AXU5EV-E FPGA controller board (**Fig. 4g**). As shown, the PCB driver is composed of a STM32F103ZET6 microcontroller unit (MCU), MUX36S06 multiplexers, OPA657 transimpedance amplifiers (TIA), LM358 TIAs, DAC5578 digital-to-analog converters (DAC) and an ADC128 analog-to-digital converter (ADC). It comprises four distinct modules of line selection, weight writing, data reading and MCU control. The module for line selection accounts for turning ON and OFF the pixels in a line-wise manner, as well as collaborates with the weight writing and data reading modules to attain precise control of the pixels. The weight writing modules reconfigure the photoresponsivity of each pixel through source-drain modulation. The data reading module receives column current outputs that represent corresponding features of the captured image, and outputs digital signal following amplification, current-to-voltage conversion *via* TIAs, filtering, and analog-to-digital conversion by ADC units. MCU controls all operations of the entire system, including the data transmission between the RSA and PCB driver using the flexible printed cable (FPC) connection, as well as that between the PCB driver and the FPGA controller through universal synchronous/asynchronous receiver/transmitter (USART) protocol. The software of the system control program and hardware circuit of the three-layer fully-connected neural network are burnt into the MCU unit and the FPGA controller board, respectively.

In summary, we incorporated the ODFE algorithm into the FOPR-Net to simultaneously execute feature and encode information from the generic representation of the captured visual scenario. The ODFE algorithm effectively simplifies the feature extraction process and enables its execution within visual sensor arrays, while the necessity of using digital circuits to perform subsequent target recognition is still a limitation not just of our study but current state of retinomorphic computing with novel optoelectronic devices. This reliance stems from the complexity of high-level cognitive tasks such as classification and decision-making, which require advanced computational

capabilities that are presently beyond the scope of optoelectronic devices. Digital circuits offer the flexibility and processing power needed to handle these tasks efficiently. We highlight that integrating more advanced computational functionalities directly into optoelectronic devices is a significant challenge and an active area of future research. Future developments could focus on: (1) Hybrid Systems: Developing hybrid architectures that synergistically combine optoelectronic devices for parallel, low-power feature extraction with digital circuits for complex processing tasks. (2) Neuromorphic Computing: Exploring neuromorphic hardware implementations that mimic neural architectures, potentially allowing more of the recognition process to occur within the sensor array itself. (3) Material Innovations: Investigating new materials and device structures that support higher-order processing capabilities, potentially reducing dependence on external digital circuits. (4) All-Optical Computing: Advancing all-optical computing technologies, which could enable both sensing and processing functions within an optical framework to minimize electronic domain bottlenecks. We believe that addressing these challenges is crucial for the evolution of retinomorphic computing systems. By outlining these future directions, we aim to provide a broader perspective on how the field can progress toward fully integrated retinomorphic systems that minimize reliance on traditional digital circuits.

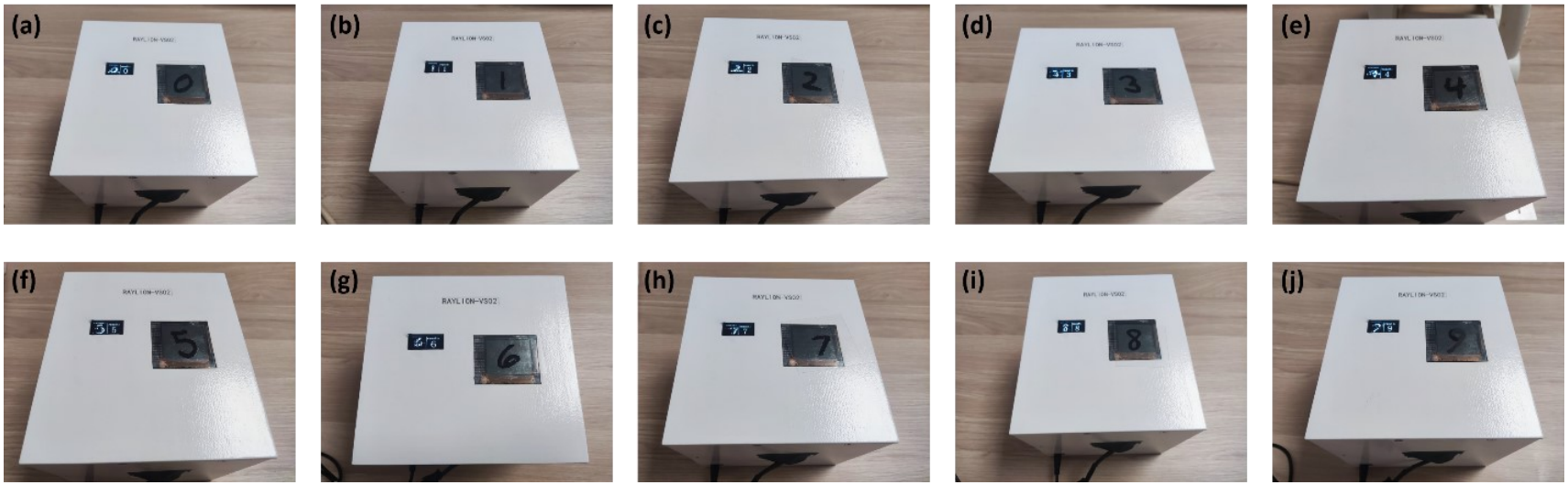

Fig. S26. Photographs of handwritten digit images recognition using the perovskite retinomorphic hardware system. Handwritten digit (a) “0”, (b) “1”, (c) “2”, (d) “3” (e) “4”, (f) “5”, (g) “6”, (h) “7”, (i) “8” and (j) “9”.

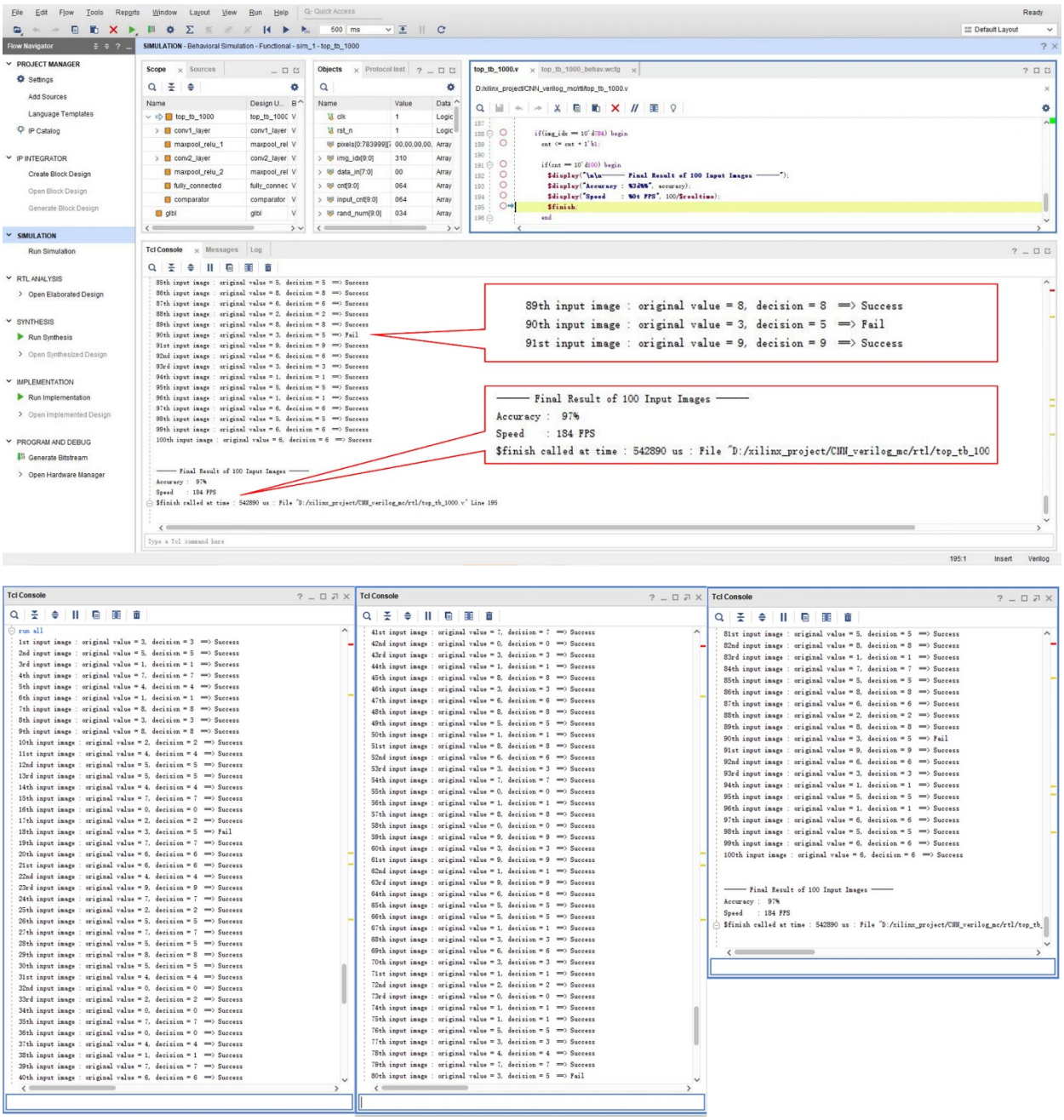

Fig. S27. Response time of the retinomorphic system. Running results of the perovskite retinomorphic hardware system for processing 100 sets of MNIST handwritten digit images.

8. Embodied intelligent vision for exoskeleton robot

When the flashing counting-down numbers of the traffic light are 4 or 3, with the initial speed of 1 m/s and distance of 5 m from the traffic junction, the exoskeleton robot is unable to pass through safely. Therefore, it has to accelerate to a speed lower than the safety limit of 2.5 m/s. Let us assume that the robot just crosses the junction when the flashing timer counts to 0 and the traffic light turns to red. According to the follow equations

$$V_t = V_0 + at \tag{14}$$

$$d = V_0 t + \frac{1}{2} a t^2 \tag{15}$$

where V_t is the final speed of the robot after acceleration, V_0 is its initial speed of 1 m/s, a is the acceleration speed, t is the counting-down time, and d is the distance of 5 m from the traffic junction, the acceleration and final speed should be no less than (1/8 m/s^2, 1.5 m/s) and (4/9 m/s^2, 7/3 m/s) for counting-down time of 4 and 3 s, respectively.

When the flashing counting-down numbers of the traffic light are 2 or 1, with the initial speed of 1 m/s and distance of 5 m from the traffic junction, the exoskeleton robot is in no way able to pass through the crossroad under the speed limit of 2.5 m/s. Therefore, it has to decelerate to stop before the stop line and wait for the traffic light to turn into green again. According to the follow equations

$$V_t = V_0 - at \tag{16}$$

$$d = V_0 t - \frac{1}{2} a t^2 \tag{17}$$

where V_t is the final speed of 0 after deceleration, V_0 is its initial speed of 1 m/s, a is the deceleration speed, t is the counting-down time, and d is the braking distance no more than 5 m from the traffic junction, the deceleration speed should be no less than -0.1 m/s^2 for the robot to stop safely.

In order to compose the database used for FO-RNN's training, we use various electronic digits of 9 to 0 with different contrast and noise levels in black grounds to represent the counting-down numbers of the flashing traffic light timer that are recorded in the morning, at noon, or in the evening. As shown

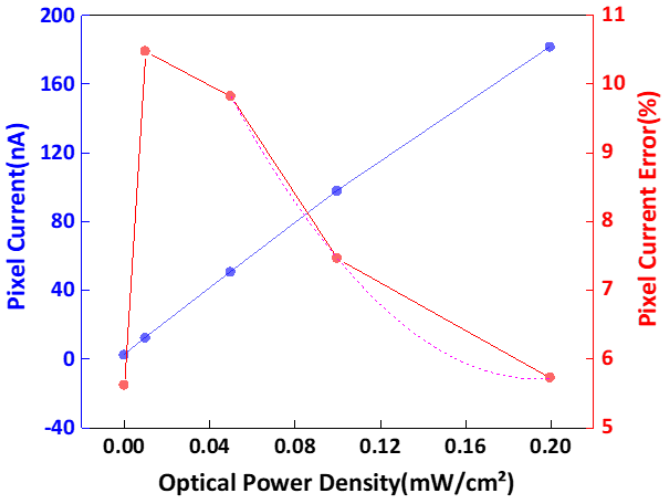

Fig. S28. Pixel current and corresponding errors. Average values and errors of the photocurrents recorded in all 4096 pixels of the perovskite RSA as a function of the optical illumination intensities.

in Fig. S28, the average pixel photocurrents of the perovskite RSA increase monotonically and linearly with the illuminating light intensities, while the variations of the pixel photocurrents over the entire 4096-pixel array decreases accordingly. Note that as the exoskeleton robot approaches nearer to the crossroad, the intensities of the traffic light timer projected onto the perovskite RSA increase. The brightness and clarity of the recorded electronic digits should also increase. Following the linear relationship between the average pixel photocurrents and optical power densities plotted in Fig. S28, the absolute brightness of the electronic digits recorded at the last time-step T_5 is defined as pure white of 255, while that of the backgrounds monitored at the same time-step is taken as pure black of 0. In accordance, the brightnesses of the electronic digits obtained at previous time-steps T_0 ~T_4 are adjusted proportionally. In the meanwhile, the black backgrounds maintain their brightnesses of 0 for all time steps. The above case describes the database preparation philosophy for that obtained under normal light conditions with optical power density of 0.2 mW/cm^2 in the morning (middle panel of **Fig. 5b**). As for the case monitored during noon period, we assume that the optical power density and respective average pixel photocurrents increase by 200% in comparison to those recorded in the morning. Therefore, the brightnesses of the black backgrounds are adjusted to 255/3=85, while those of the electronic digits decrease to 1/3 of their

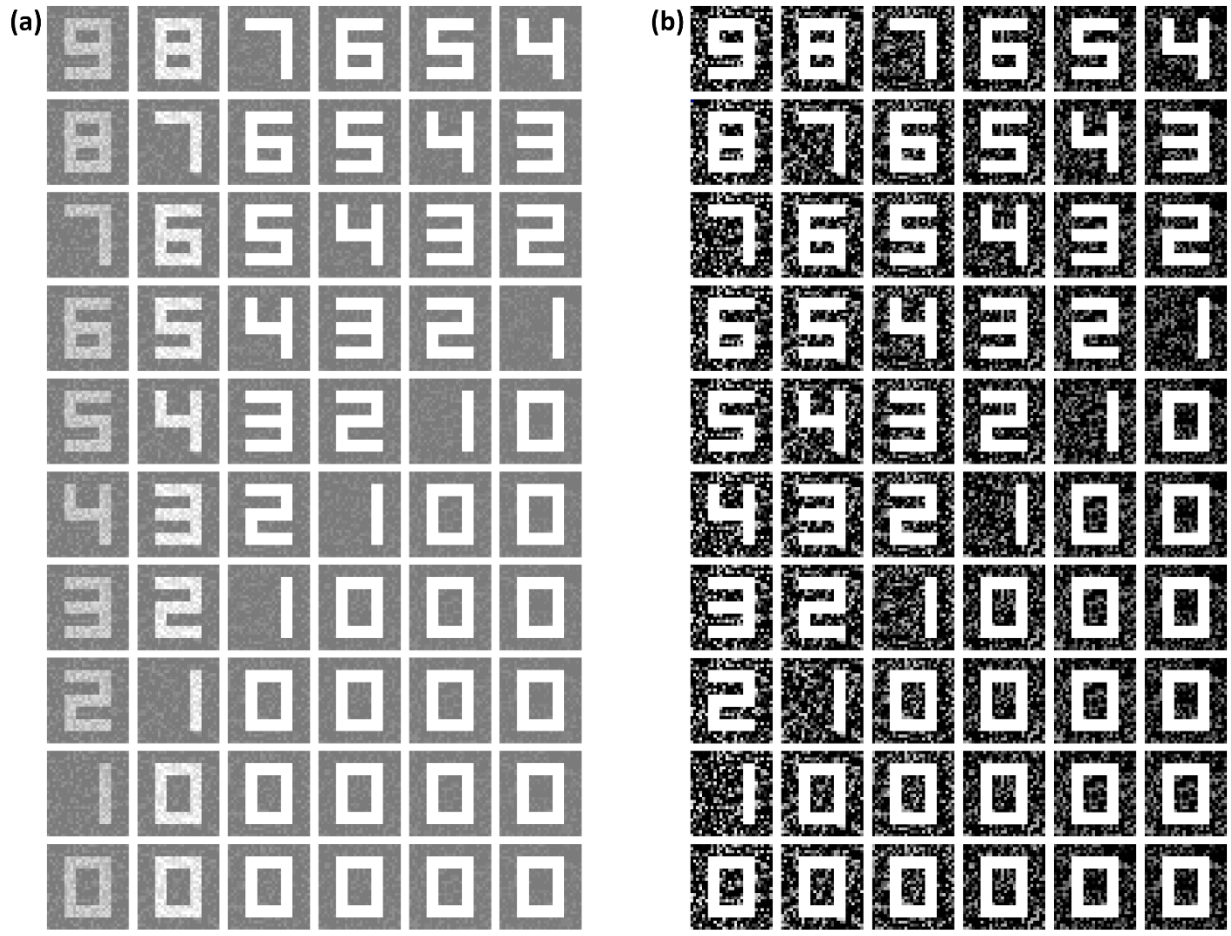

Fig. S29. Database of the counting-down numbers of flashing traffic light timer. (a) at noon and (b) in the evening, for neural network training and prediction of FO-RNN.

original values, respectively (Fig. S29a). It should be pointed that as device-to-device deviations (Errors) exist in the photocurrents of the 4096 pixels over the entire perovskite RSA, the monitored images of the flashing traffic light timer also contain noises. As fitted in Fig. S29, the average pixel photocurrent errors and noises over the 4096-pixel array can be derived according to the following equations

$$Error = 0.13 - 0.77P_{light} + 1.98(P_{light})^2 \quad (18)$$

$$noise = 255 \times Error \quad (19)$$

where P_{light} is the optical power density. Consequently, the noises appeared on each image of the counting-down numbers are added as

$$IMG\_NOISE_{T_n} = IMG_{T_n} + [U(-noise, noise)]_{64\times64} \quad (20)$$

where $IMG\_NOISE_{T_n}$ is the image of the flashing traffic light timer recorded at time step T_n with noise, whereas $[U(\text{-}noise, noise)]_{64\times64}$ represents the uniformly distributed random noise added onto each pixel of the image in the range of (*-noise, noise*), according to the function

$$random.uniform(a, b) \quad (21)$$

where a equals to -noise and b equals to noise. In the evening, although the optical power density decreases by 50% to 0.1 mW/cm^2, the brightnesses of the black backgrounds can only maintain their lowest level of 0 unchanged. Nevertheless, the brightnesses of their noises decrease to 50% of those recorded in the morning accordingly. On the other hand, the brightnesses of the electronic digits also decrease to 50% of the original values recorded in the morning, with their noises disappearing completely. The imaging contrasts of the monitored flashing traffic light timer thus increase by 100%, respectively (Fig. S29b). As such, the database for FO-RNN's training is established. Totally 9000 and 900 subgroups of electronic digits are included in the database, wherein each subgroup contains 6 images of the electronic digits arranged in a monotonically decreasing sequence. The database is further divided into 3000 and 300 subgroups for the motion statues of L_1, L_2 and L_3, respectively. Fig. S30 displays the confusion matrices, obtained after 50 training epochs, for the FO-RNN to make decisions on the exoskeleton robot's motion across the traffic junction during different time periods over a day. As shown, high accuracies exceeding 93.3% can be achieved by the retinomorphic computation and exoskeleton robot either in the morning, at noon or in the evening.

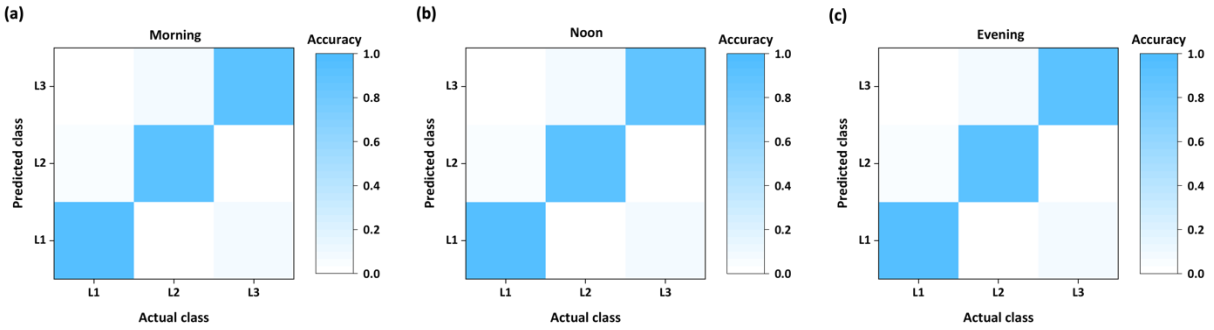

Fig. S30. Confusion matrices for the FO-RNN and retinomorphic computing system. The results obtained over 50 training epochs to make decisions on the exoskeleton robot's motion across the traffic junction (a) in the evening, (b) at noon and (c) in the evening, respectively.

Movie S1. Calibration of the perovskite RSA in dark and under white light illumination of different intensities.

Movie S2. Image sensing of various objects using the perovskite RSA.

Movie S3. Image sensing of handwritten digits under white light illumination of different intensities using the perovskite RSA.

Movie S4. Adaptive image sensing of handwritten digits under weak white light illumination upon photoresponsivity reconfiguration of the perovskite RSA.

Movie S5. Image sensing of handwritten digits under monochromic illumination at different wavelength using the perovskite RSA.

Movie S6. Image sensing of handwritten digits covered by printing paper under red and NIR illumination using the perovskite RSA.

Movie S7. Recognition of handwritten digits using the perovskite RSA and unpacked retinomorphic system.

Movie S8. Recognition of handwritten digits using the perovskite RSA based prototype retinomorphic system.

REFERENCES AND NOTES

1. L. Gionfrida, D. Kim, D. Scaramuzza, D. Farina, R. D. Howe, Wearable robots for the real world need vision. *Sci. Robot.* **9**, eadj8812 (2024).

2. H. Xia, Y. Zhang, N. Rajabi, F. Taleb, Q. Yang, D. Kragic, Z. Li, Shaping high-performance wearable robots for human motor and sensory reconstruction and enhancement. *Nat. Commun.* **15**, 1760 (2024).

3. D. Kim, B. B. Kang, K. B. Kim, H. Choi, J. Ha, K. Cho, S. Jo, Eyes are faster than hands: A soft wearable robot learns user intention from the egocentric view. *Sci. Robot.* **4**, eaav2949 (2019).

4. G. Underwood, Reptilian retinas. *Nature* **167**, 183–185 (1951).

5. P. S. Gehring, *Leaf-tailed Geckos—The Complete Uroplatus* (Edition Chimaira, 2020).

6. R. Llinas, W. Precht, *Neurophysiology of the Anuran Visual System in Frog Neurobiology, A Handbook* (Springer, 1976).

7. K. Donner, C. A. M. Yovanovich, A frog's eye view: Foundational revelations and future promises. *Semin. Cell Dev. Biol.* **106**, 72–85 (2020).

8. T. Gollisch, M. Meister, Eye smarter than scientists believed: Neural computations in circuits of the retina. *Neuron* **65**, 150–164 (2010).

9. F. Zhou, Y. Chai, Near-sensor and in-sensor computing. *Nat. Electron.* **3**, 664–671 (2020).

10. J. Michel, J. Liu, L. C. Kimerling, High-performance Ge-on-Si photodetectors. *Nat. Photon.* **4**, 527–534 (2010),.

11. P. Cheben, R. Halir, J. H. Schmid, H. A. Atwater, D. R. Smith, Subwavelength integrated photonics. *Nature* **560**, 565–572 (2018).

12. P. Martyniuk, P. Wang, A. Rogalski, Y. Gu, R. Jiang, F. Wang, W. Hu, Infrared avalanche photodiodes from bulk to 2D materials. *Light Sci. Appl.* **12**, 212 (2023).

13. S. Seo, S. Jo, S. Kim, J. Shim, S. Oh, J. Kim, K. Heo, J. Choi, C. Choi, S. Oh, D. Kuzum, H.-S. P. Wong, J. Park, Artificial optic-neural synapse for colored and color-mixed pattern recognition. *Nat. Commun.* **9**, 5106 (2018).

14. L. Mennel, J. Symonowicz, S. Wachter, D. K. Polyushkin, A. J. Molina-Mendoza, T. Mueller, Ultrafast machine vision with 2D material neural network image sensors. *Nature* **579**, 62–66 (2020).

15. C. Wang, S. Liang, S. Wang, P. Wang, Z. Li, Z. Wang, A. Gao, C. Pan, C. Liu, J. Liu, H. Yang, X. Liu, W. Song, C. Wang, B. Cheng, X. Wang, K. Chen, Z. Wang, K. Watanabe, T. Taniguchi, J. J. Yang, F. Miao, Gate-tunable van der Waals heterostructure for reconfigurable neural network vision sensor. *Sci. Adv.* **6**, eaba6173 (2020).

16. C. Choi, J. Leem, M. Kim, A. Taqieddin, C. Cho, K. W. Cho, G. J. Lee, H. Seung, H. J. Bae, Y. M. Song, T. Hyeon, N. R. Aluru, S. Nam, D. Kim, Curved neuromorphic image sensor array using a MoS_2-organic heterostructure inspired by the human visual recognition system. *Nat. Commun.* **11**, 5934 (2020).

17. L. Tong, Z. Peng, R. Lin, Z. Li, Y. Wang, X. Huang, K. Xue, H. Xu, F. Liu, H. Xia, P. Wang, M. Xu, W. Xiong, W. Hu, J. Xu, X. Zhang, L. Ye, X. Miao, 2D materials-based homogeneous transistor-memory architecture for neuromorphic hardware. *Science* **373**, 1353–1358 (2021).

18. L. Pi, P. Wang, S. Liang, P. Luo, H. Wang, D. Li, Z. Li, P. Chen, X. Zhou, F. Miao, T. Zhai, Broadband convolutional processing using band-alignment-tunable heterostructures. *Nat. Electron.* **5**, 248–254 (2022).

19. Z. Zhang, S. Wang, C. Liu, R. Xie, W. Hu, P. Zhou, All-in-one two-dimensional retinomorphic hardware device for motion detection and recognition. *Nat. Nanotechnol.* **17**, 27–32 (2022).

20. J. Meng, T. Wang, H. Zhu, L. Ji, W. Bao, P. Zhou, L. Chen, Q. Sun, D. W. Zhang, Integrated in-sensor computing optoelectronic device for environment-adaptable artificial retina perception application. *Nano Lett.* **22**, 81–89 (2022).

21. G. Zhang, Z. Zhang, X. Chen, L. Kang, Y. Li, F. Wang, L. Shi, K. Shi, Z. Liu, J. Tian, T. Lu, J. Zhang, Broadband sensory networks with locally stored responsivities for neuromorphic machine vision. *Sci. Adv.* **9**, eadi5104 (2023).

22. X. Fu, T. Li, B. Cai, J. Miao, G. N. Panin, X. Ma, J. Wang, X. Jiang, Q. Li, Y. Dong, C. Hao, J. Sun, H. Xu, Q. Zhao, M. Xia, B. Song, F. Chen, X. Chen, W. Lu, W. Hu, Graphene/$MoS_{2-x}O_x$/graphene photomemristor with tunable non-volatile responsivities for neuromorphic vision processing. *Light Sci. Appl.* **12**, 39 (2023).

23. G. Wu, X. Zhang, G. Feng, J. Wang, K. Zhou, J. Zeng, D. Dong, F. Zhu, C. Yang, X. Zhao, D. Gong, M. Zhang, B. Tian, C. Duan, Q. Liu, J. Wang, J. Chu, M. Liu, Ferroelectric-defined reconfigurable homojunctions for in-memory sensing and computing. *Nat. Mater.* **22**, 1499–1506 (2023).

24. X. Pan, J. Shi, P. Wang, S. Wang, C. Pan, W. Yu, B. Cheng, S. Liang, F. Miao, Parallel perception of visual motion using light-tunable memory matrix. *Sci. Adv.* **9**, eadi4083 (2023).

25. Y. Zhou, J. Fu, Z. Chen, F. Zhuge, Y. Wang, J. Yan, S. Ma, L. Xu, H. Yuan, M. Chan, X. Miao, Y. He, Y. Chai, Computational event-driven vision sensors for in-sensor spiking neural networks. *Nat. Electron.* **9**, 870–878 (2023).

26. P. Huang, B. Jiang, H. Chen, J. Xu, K. Wang, C. Zhu, X. Hu, D. Li, L. Zhen, F. Zhou, J. Qin, C. Xu, Neuro-inspired optical sensor array for high-accuracy static image recognition and dynamic trace extraction. *Nat. Commun.* **14**, 6736 (2023).

27. D. Xiang, T. Liu, J. Xu, J. Y. Tan, Z. Hu, B. Lei, Y. Zheng, J. Wu, A. H. C. Neto, L. Liu, W. Chen, Two-dimensional multibit optoelectronic memory with broadband spectrum distinction. *Nat. Commun.* **9**, 2966 (2018).

28. H. Jang, C. Liu, H. Hinton, M. Lee, H. Kim, M. Seol, H. Shin, S. Park, D. Ham, An atomically thin optoelectronic machine vision processor. *Adv. Mater.* **32**, 2002431 (2020).

29. J. Lee, S. Tan, S. I. Seok, Y. Yang, N. Park, Rethinking the A cation in halide perovskites. *Science* **375**, 6583 (2022).

30. Y. Zhou, L. M. Herz, A. K-Y. Jen, M. Saliba, Advances and challenges in understanding the microscopic structure–property–performance relationship in perovskite solar cells. *Nat. Energy* **7**, 794–807 (2022).

31. H. Zhang, L. Pfeifer, S. M. Zakeeruddin, J. Chu, M. Gratzel, Tailoring passivators for highly efficient and stable perovskite solar cells. *Nat. Rev. Chem.* **7**, 632–652 (2023).

32. Q. Chen, Y. Zhang, S. Liu, T. Han, X. Chen, Y. Xu, Z. Meng, G. Zhang, X. Zheng, J. Zhao, G. Cao, G. Liu, Switchable perovskite photovoltaic sensors for bioinspired adaptive machine vision. *Adv. Intell. Syst.* **2**, 2000122 (2020).

33. P. Calado, A. M. Telford, D. Bryant, X. Li, J. Nelson, B. C. O'Regan, P. R. F. Barnes, Evidence for ion migration in hybrid perovskite solar cells with minimal hysteresis. *Nat. Commun.* **7**, 13831 (2016).

34. C. Eames, J. M. Frost, P. R. F. Barnes, B. C. O'Regan, A. Walsh, M. S. Islam, Ionic transport in hybrid lead iodide perovskite solar cells. *Nat. Commun.* **6**, 7497 (2015).

35. A. Senocrate, J. Maier, Solid-state ionics of hybrid halide perovskites. *J. Am. Chem. Soc.* **141**, 8382–8396 (2019).

36. Y. Yuan, Q. Wang, J. Huang, *Ion Migration in Hybrid Perovskite Solar Cells* (Springer, 2016).

37. W. Tress, N. Marinova, T. Moehl, S. M. Zakeeruddin, M. K. Nazeeruddina, M. Grätzela, Understanding the rate-dependent J-V hysteresis, slow time component, and aging in $CH_3NH_3PbI_3$ perovskite solar cells: The role of a compensated electric field. *Energ. Environ. Sci.* **8**, 995–1004 (2015).

38. Y. Zhang, M. Liu, G. E. Eperon, T. C. Leijtens, D. McMeekin, M. Saliba, W. Zhang, M. D. Bastiani, A. Petrozza, L. M. Herz, M. B. Johnston, H. Lin, H. J. Snaith, Charge selective contacts, mobile ions and anomalous hysteresis in organic–inorganic perovskite solar cells. *Mater. Horiz.* **2**, 315–322 (2015).

39. J. Zhou, H. Qiu, T. Wen, Z. He, C. Zou, Y. Shi, L. Zhu, C. Chen, G. Liu, S. Yang, F. Liu, Z. Yang, Acidity control of interface for improving stability of all-perovskite tandem solar cells. *Adv. Energy Mater.* **13**, 2300968 (2023).

40. A. Darmont, *High Dynamic Range Imaging: Sensors and Architectures* (SPIE, 2013).

41. P. Baldelli, N. Phelan, G. Egan, Investigation of the effect of anode/filter materials on the dose and image quality of a digital mammography system based on an amorphous selenium flat panel detector. *Br. J. Radiol.* **83**, 290–295 (2010).

42. E. Seeram, *Computed Tomography: Physical Principles, Clinical Applications, and Quality Control* (Elsevier Health Sciences, 2015).

43. C. H. Ye, D.-H. Lee, CMOS image sensor: Characterizing its PRNU (photo-response non-uniformity). *Proc. SPIE* **10757**, 41–47 (2018).

44. S. Kasap, P. Capper, *Springer Handbook of Electronic and Photonic Materials* (Springer, 2017), chapter 45.

45. Z. Song, X. Du, X. He, H. Wang, Z. Liu, H. Wu, H. Luo, L. Jin, L. Xu, Z. Zheng, G. Niu, J. Tang, Rheological engineering of perovskite suspension toward high-resolution X-ray flat-panel detector. *Nat. Commun.* **14**, 6865 (2023).

46. R. Lin, Y. Wang, Q. Lu, B. Tang, J. Li, H. Gao, Y. Gao, H. Li, C. Ding, J. Wen, P. Wu, C. Liu, S. Zhao, K. Xiao, Z. Liu, C. Ma, Y. Deng, L. Li, F. Fan, H. Tan, All-perovskite tandem solar cells with 3D/3D bilayer perovskite heterojunction. *Nature* **620**, 994–1000 (2023).

47. A. M. Najarian, M. Vafaie, A. Johnston, T. Zhu, M. Wei, M. I. Saidaminov, Y. Hou, S. Hoogland, F. P. G. Arquer, E. H. Sargent, Sub-millimetre light detection and ranging using perovskites. *Nat. Electron.* **5**, 511–518 (2022).

48. J. Ohta, *Smart CMOS Image Sensors and Applications* (CRC Press, 2017).

49. X. Gong, M. Tong, Y. Xia, W. Cai, J. S. Moon, Y. Cao, G. Yu, C. Shiei, B. Nilsson, A. J. Heeger, High-detectivity polymer photodetectors with spectral response from 300 nm to 1450 nm. *Science* **325**, 1665–1667 (2009).

50. R. Chang, Q. Chen, W. Shen, Y. Zhang, B. Zhang, S. Wang, Controllable switching between highly rectifying schottky and p-n junctions in an ionic MoS_2 device *Adv. Funct. Mater.* **33**, 2301010 (2023).

51. S. Chen, Y. Fu, M. Ishaq, C. Li, D. Ren, Z. Su, X. Qiao, P. Fan, G. Liang, J. Tang, Carrier recombination suppression and transport enhancement enable high-performance self-powered broadband Sb_2Se_3 photodetectors. *InfoMat.* **5**, e12400 (2023).

52. Y. Lu, T. Chen, N. Mkhize, R. Chang, Y. Sheng, P. Holdway, H. Bhaskaran, J. H. Warner, GaS:WS_2 heterojunctions for ultrathin two-dimensional photodetectors with large linear dynamic range across broad wavelengths. *ACS Nano* **15**, 19570–19580 (2021).

53. D. Luo, R. Su, W. Zhang, Q. Gong, R. Zhu, Minimizing non-radiative recombination losses in perovskite solar cells. *Nat. Rev. Mater.* **5**, 44–60 (2020).

54. Y. Li, Z. Chen, B. Yu, S. Tan, Y. Cui, H. Wu, Y. Luo, J. Shi, D. Li, Q. Meng, Efficient, stable formamidinium-cesium perovskite solar cells and minimodules enabled by crystallization regulation. *Joule* **6**, 676–689 (2022).

55. Z. Yang, Z. Yu, H. Wei, X. Xiao, Z. Ni, B. Chen, Y. Deng, S. N. Habisreutinger, X. Chen, K. Wang, J. Zhao, P. N. Rudd, J. J. Berry, M. C. Beard, J. Huang, Enhancing electron diffusion length in narrow-bandgap perovskites for efficient monolithic perovskite tandem solar cells, *Nat. Commun.* **10**, 4498 (2019).

56. Z. Yu, J. Wang, B. Chen, M. A. Uddin, Z. Ni, G. Yang, J. Huang, Solution processed ternary tin (II) alloy as hole-transport layer of Sn-Pb perovskite solar cells for enhanced efficiency and stability. *Adv. Mater.* **34**, 676–689 (2022).

57. J. Cao, H. Loi, Y. Xu, X. Guo, N. Wang, C. Liu, T. Wang, H. Cheng, Y. Zhu, M. G. Li, W. Wong, F. Yan, High-performance tin-lead mixed-perovskite solar cells with vertical compositional gradient, *Adv. Mater.* **34**, e2107729 (2022).

58. Y. Zhang, S. He, W. Guo, Y. Hu, J. Huang, J. R. Mulcahy, W. D. Wei, Surface-plasmon-driven hot electron photochemistry. *Chem. Rev.* **118**, 2927–2954 (2018).

59. Z. Ni, H. Jiao, C. Fei, H. Gu, S. Xu, Z. Yu, G. Yang, Y. Deng, Q. Jiang, Y. Liu, Y. Yan, J. Huang, Evolution of defects during the degradation of metal halide perovskite solar cells under reverse bias and illumination. *Nat. Energy* **7**, 65–73 (2022).

60. Y. Lin, B. Chen, Y. Fang, J. Zhao, C. Bao, Z. Yu, Y. Deng, P. N. Rudd, Y. Yan, Y. Yuan, J. Huang, Excess charge-carrier induced instability of hybrid perovskites. *Nat. Commun.* **9**, 4981 (2018).